

# Reflectance study of ice and Mars soil simulant associations – II. CO<sub>2</sub> and H<sub>2</sub>O ice.

Zuriñe Yoldi<sup>1\*</sup>, Antoine Pommerol<sup>1</sup>, Olivier Poch<sup>1,2</sup>, Nicolas Thomas<sup>1</sup>

<sup>1</sup>*Physikalisches Institut, Universität Bern and NCCR PlanetS, Sidlerstrasse 5, 3012 Bern, Switzerland.*

<sup>2</sup>*Univ. Grenoble Alpes, CNRS, IPAG, 38000 Grenoble, France*

\* *Now at the section for the Physics of Ice, Climate and Earth at the Niels Bohr Institute, University of Copenhagen.*

---

## Abstract

We measure the visible and near-infrared reflectance of icy analogues of the Martian surface made of CO<sub>2</sub> ice associated in different ways with H<sub>2</sub>O ice and the regolith simulant JSC Mars-1. Such experimental results obtained with well-controlled samples in the laboratory are precious to interpret quantitatively the imaging and spectral data collected by various Mars orbiters, landers and rovers. Producing and maintaining well-characterized icy samples while acquiring spectro-photometric measurements is however challenging and we discuss some of the difficulties encountered in preparing and measuring our samples. We present the results in the form of photometric and spectral criteria computed from the spectra and plotted as a function of the composition and physical properties of the samples. Consistent with previous studies, we find that when intimately mixed with other materials, including water ice, CO<sub>2</sub> ice becomes rapidly undetectable due to its low

---

\*<https://doi.org/10.1016/j.icarus.2022.115116>

absorptivity. As low as 5 wt.% of fine-grained H<sub>2</sub>O ice is enough to mask entirely the signatures of CO<sub>2</sub>. Similarly, sublimation experiments performed with ternary mixtures of CO<sub>2</sub> ice, H<sub>2</sub>O ice and JSC Mars-1 show that water, even when present as a minor component (3 wt.%), determines the texture and evolution of the mixtures. We assess the ability of various combinations of spectral parameters to identify samples with H<sub>2</sub>O, CO<sub>2</sub>, JSC Mars-1, or various mixtures from their reflectance and orient our study to helping interpret ice and soil reflectance spectra from the Martian surface. From the laboratory spectra, we simulate the colour signal generated by the CaSSIS instrument to allow for direct comparisons with results from this instrument and provide to databases the necessary spectral data to perform the same operations with other instruments.

*Keywords:* Reflectance, CO<sub>2</sub> ice, Mixture, Mars, H<sub>2</sub>O ice, Polar Caps

---

## 1. Introduction

### 1.1. *CO<sub>2</sub> ice and the martian CO<sub>2</sub> cycle*

Solid carbon dioxide (CO<sub>2</sub> ice) is present at the surface of various bodies of the Solar System, such as comet 67P-CG [1], Triton [2] or Mars. In the case of Mars, where it represents 96% of the atmosphere [3], CO<sub>2</sub> drives the condensation flow [4]: as a result of the current obliquity of Mars ( $\sim 25^\circ$ ), its hemispheres do not receive the same amount of sunlight, which results in seasonal differences of temperature and pressure conditions in each hemisphere. As a consequence, a large fraction of the atmosphere moves seasonally from the summer hemisphere to the winter hemisphere and back. Almost a quarter of the atmosphere condenses in winter [5], sublimates during spring and migrates to the other hemisphere, where it condenses again to continue the cycle. Beside the CO<sub>2</sub> cycle [6], H<sub>2</sub>O [7] and dust [8] cycles happen yearly within the Martian atmosphere. CO<sub>2</sub> frost has also been detected at all latitudes on Mars [9].

In 1971, Neugebauer et al. [10] confirmed with Mariner 6 and 7 data the predictions previously made by Leighton and Murray [11]: the southern seasonal cap was made of CO<sub>2</sub>. Since then, the community has grown a broad knowledge of the CO<sub>2</sub> and H<sub>2</sub>O condensation/sublimation processes by monitoring the high-latitude regions of Mars with multiple techniques (e.g., gravimetry, gamma-ray and neutron spectrometer, laser altimetry, reflectance spectroscopy or temperature measurements). We know that at the martian mid-to-high latitudes, water ice starts condensing as autumn arrives, first as night-time frost and later as seasonal frost. Once in autumn, the condensation temperature of CO<sub>2</sub> is attained at the surface (150K at 6

mbar), causing CO<sub>2</sub> to directly condense on the regolith, or in the atmosphere, causing solidified CO<sub>2</sub> to deposit as frost. In the latter case, CO<sub>2</sub> can nucleate around atmospheric particles of water ice or dust, resulting in the cleaning of the atmosphere and contaminated CO<sub>2</sub> ice at the surface. As spring starts, the first light from the Sun causes the seasonal deposits to sublimate, first the CO<sub>2</sub> and then H<sub>2</sub>O. By mid-summer, all the seasonal deposits have sublimated.

### *1.2. Parameters controlling the reflectance - Models*

Comparisons of the optical constants of H<sub>2</sub>O and CO<sub>2</sub> ices [12, 13, 14, 15] already suggest that their spectro-photometric properties will be relatively similar with very low absorption in the visible spectral range and intense and wide absorption bands in the near- to mid-infrared. Different types of radiative transfer models and numerical simulations [16, 17, 18, 19, 20] can then be used to compute the reflectance of a parameterized surface made of the ices, pure or mixed with contaminants, from their optical constants. The relevant parameters are related to both the individual grains (size, shape, surface texture, internal defects and inclusions...) and the macroscopic properties of the surface (density, roughness...). Because of the similarity of their optical properties, a lot of what is known about water ice can be extrapolated to carbon dioxide ice while one keeping an eye on the known differences.

The physical size of the ice articles plays a very large role in the reflectance of icy surfaces. In the visible spectral range, fine grained ( $\lesssim 100 \mu\text{m}$ ) frost and snow made of both CO<sub>2</sub> and H<sub>2</sub>O in their pure form present a very high reflectance and thin ( $\lesssim 1 \text{ cm}$ ) layers are sufficient to hide the substrate and reflect nearly 100% of the incident light. The bidirectional

reflectance behaviour of water snow is also observed to be nearly lambertian, i.e. the measured radiance does not depend on the position of the observer and shows a cosine dependence on the light incidence angle. Coarse grained and compact ice however can transmit the light to large depth and the effects of absorption can be observed because of the long optical path. This gives rise for instance to the blue colour of the compact ice in glaciers as the absorption index of H<sub>2</sub>O increases with wavelength. In the near- and mid- infrared spectra of both H<sub>2</sub>O and CO<sub>2</sub>, the depths of the absorption bands are strongly influenced by particle size and the most intense bands saturate for coarse grained and compact ice. Note that CO<sub>2</sub> displays sharper and less intense infrared absorption bands than H<sub>2</sub>O overall resulting in a significantly higher albedo for a given particle size [19].

Beside particle size, the other parameter which strongly influences the reflectance of icy surfaces is the presence of contaminants, even in trace amount and the way they are aggregated with the ice (intimate or geographic mixtures, coating at the surface of the grains...). It has already been shown in a variety of contexts that tiny amounts of dark contaminants are sufficient to hide the photometric signatures of water ice. For instance, Yoldi et al. [21] show experimentally that intimate mixtures of fine grained basalt powder and coarser grained water ice do not appear brighter than the pure basalt powder even with three times more ice than basalt in the mixture. Khuller et al. [20] model binary mixtures of water ice and Martian dust and find that less than 1 wt% of dust mixed with fine grained ice can reduce its albedo by a factor of 10.

### *1.3. Observations of CO<sub>2</sub> ice in the southern hemisphere*

In the southern Martian hemisphere, a small and thin ( $< 20$  m) permanent cap of CO<sub>2</sub> ice [22] covers part of a much larger km-thick unit known as the South Polar Layered Deposits (SPLD). This unit is made essentially of water ice mixed with dust [23, 24] but some ancient and massive deposits of carbon dioxide ice have also been found [25]. The water ice is exposed at a few places, notably along scarps [23, 26] but is otherwise covered by a desiccated dust layer.

In winter, seasonal ice deposits extend well beyond the limits of the SPLD to reach a latitude of about 50 degrees and recede during spring until only the permanent CO<sub>2</sub> cap is left in Summer. Calvin and Martin [27] and later on Kieffer et al. [28] studied the evolution of the southern seasonal cap to discover that it was controlled by CO<sub>2</sub> grain size. They found both long and short optical path lengths, compatible with ice slabs (metres) and smaller (centimetres) grains of CO<sub>2</sub> ice, respectively. The size of the CO<sub>2</sub> ice grains is the primary cause for albedo variations. The presence of translucent slab ice in the so-called cryptic region at the beginning of spring is also hypothesised to be the reason for the intense jet activity observed and attributed to solid state greenhouse effect within the layer of translucent CO<sub>2</sub> ice [29].

Langevin et al. [30] used the Observatoire pour la Minéralogie, l'Eau, les Glaces, et l'Activité (OMEGA) on Mars Express to monitor the evolution of the southern seasonal cap from the southern winter solstice to mid-summer. The observations were consistent with the presence of transparent CO<sub>2</sub> slabs but also locally with events related to the sublimation and re-condensation of water ice. With the Compact Reconnaissance Imaging Spectrometer for

Mars (CRISM, Murchie et al. [31]) and the Mars Color Imager (MARCI, Bell et al. [32]), on Mars Reconnaissance Orbiter, Brown et al. [33] confirmed the presence of pure water ice deposits during the final stages of the recession of the southern seasonal cap. They also inferred CO<sub>2</sub> grain sizes of up to 70 ± 10 mm before the springtime sublimation of the cap, and of 2.5-5 ± 1 mm in the residual cap. Using CRISM and the High Resolution Imaging Science Experiment (HiRISE, McEwen et al. [34]), Pommerol et al. [35] monitored the evolution of the south polar layered deposits from spring to summer. Around  $L_s \sim 250$  degrees, shortly before the southern summer, they observe an increase of both the albedo and the strength of the CO<sub>2</sub> ice bond strength, which they attribute to a cleaning of the icy deposits as they sublimate.

Brown et al. [36] studied, with CRISM, the origin of the water ice signature that had been repeatedly noticed at the southern cap during summer. They linked this signature with the deposition of atmospheric H<sub>2</sub>O ice on the cap. They assessed this deposition to an equivalent H<sub>2</sub>O layer of 0.2 mm and 70% porosity (0.013 g/cm<sup>2</sup>).

#### *1.4. Observations of CO<sub>2</sub> ice in the northern hemisphere*

Contrary to the southern hemisphere where the SPLD are almost entirely buried below an optically thick layer of dust and the small CO<sub>2</sub> cap, the Northern Polar layered Deposits (NPLD) expose a vast surface of water ice to the atmosphere. This has important consequences for seasonal evolution of northern polar regions. While overall the seasonal processes are relatively similar in both hemisphere, significant differences exist. In particular, the seasonal deposits in the northern hemisphere contain much more water ice than in the southern hemisphere. Using THEMIS [37] and TES

[38] data, Wagstaff et al. [39] identified and characterized the seasonal water ice annulus first hypothesised by [40]. Langevin et al. [41] monitored with OMEGA the composition of the northern latitudes of Mars. They linked albedo changes in early summer with an increase in the size of the ice grains. They also assessed the dust content within the ice to be low (a maximum of 5% if intimate mixtures and  $\ll 1\%$  if intramixtures). Appéré et al. [42] used the same instrument to study the retreat of the north seasonal deposits during two consecutive Martian years, and mapped the temporal and spatial distributions of CO<sub>2</sub> and H<sub>2</sub>O ice. They observed CO<sub>2</sub> winter condensation compatible with transparent slabs, surrounded by the water ice annulus. This annulus consisted first of thin frost and was later covered by water ice grains that were previously trapped in CO<sub>2</sub>. This surficial water-rich layer dominated the reflectance spectra of the deposits around  $L_S=50^\circ$ , even though the CO<sub>2</sub> locally reappeared between  $L_S=50^\circ$  and  $L_S=70^\circ$ .

Hansen et al. [43], Portyankina et al. [44] and Pommerol et al. [45] studied dynamic processes in the northern seasonal polar cap by analysing HiRISE images. Hansen et al. [43] and Portyankina et al. [44] showed that sublimation process play an active role in the erosion of dunes. They conclude that the same model which explains dynamic southern sublimation processes [29] is also applicable to fans and dark spots over dunes fields observed in the northern hemisphere. Pommerol et al. [45] confirmed with CRISM data the local reappearances of the CO<sub>2</sub> spectral signatures in late spring first seen by Appéré et al. [42] and hypothesize that the removal of surficial water frost by local winds explains this evolution.

### *1.5. Laboratory measurements of CO<sub>2</sub> ice and H<sub>2</sub>O ice mixtures*

Numerical models can be used to establish the properties of the polar surfaces (see section 1.2). Many experiments have also been conducted on thin films and single crystals to measure transmission spectra of pure CO<sub>2</sub> ice or mixtures with H<sub>2</sub>O [46, 47]. However, there is a lack of measured reflectance data with macroscopic and well-controlled and documented CO<sub>2</sub>-ice samples, which are needed to calibrate the models and validate the interpretations. This is explained by the technical challenges that working with large amounts of CO<sub>2</sub> ice entails: for example, its fast sublimation and the over-pressure that it might induce if enclosed or its propensity to cold trap water frost from the atmosphere. We summarise here the most relevant experimental studies on the reflectance of CO<sub>2</sub> ice.

In the late 60s, Kieffer [48, 49] carried out the first laboratory studies on the spectral reflectance of CO<sub>2</sub> and H<sub>2</sub>O frosts in the near- to mid- infrared (0.8 - 3.2  $\mu\text{m}$ ). By introducing gas of controlled composition into a cold chamber, he condensed the water and carbon dioxide on the walls and measured their reflectance from 0.8 to 3.2  $\mu\text{m}$ . He observed a masking of the CO<sub>2</sub> signatures by H<sub>2</sub>O, thus concluding that a CO<sub>2</sub>-free reflectance spectrum does not discard the presence of CO<sub>2</sub>. While the resolution and quality of the data in the (1.7 - 3.0  $\mu\text{m}$ ) range are sufficient for comparison with orbital data, the spectral resolution in the (0.8 - 1.7)  $\mu\text{m}$  range is very coarse and does not allow to resolve the fine CO<sub>2</sub> features. The reflectance was not measured in the visible range, shortward of 0.8  $\mu\text{m}$ . Despite these issues, this unique data set remains one of the best sources of information on the spectral reflectance of CO<sub>2</sub> ice, half a century after its collection.

Similar to Kieffer [49], Bernstein et al. [50] mixed carbon dioxide and water in their gaseous phases and condensed them to grow frost. They observed a possible enhancement of a CO<sub>2</sub> feature at 2.135  $\mu\text{m}$  in mixtures of CO<sub>2</sub> with other materials, which they pointed out as a potential indicator of the presence of CO<sub>2</sub> in mixtures. In the absence of pictures, it is understood that the samples assessed in their study are thin layers of ice.

Oancea et al. [51] measured infrared reflectance spectra of mixtures between CO<sub>2</sub> and H<sub>2</sub>O to study specifically the spectroscopic signal of CO<sub>2</sub> clathrate hydrates. They identified two bands of the clathrate at 2.71 and 4.28  $\mu\text{m}$  which can be used for the identifications of such clathrates in remote-sensing data.

The team from IPAG (Institut de Planétologie et d'Astrophysique de Grenoble) has also presented reflectance measurements of different mixtures of CO<sub>2</sub> and H<sub>2</sub>O ices. Grisolle et al. [52] condensed various thicknesses of water frost on a sample of CO<sub>2</sub> snow and studied its reflectance between 1.3-1.7  $\mu\text{m}$ . Philippe et al. [53] and Schmitt et al. [54] have performed sublimation experiments with polycrystalline translucent CO<sub>2</sub> ice and dust and have shown that dust sinking and slab cracking only produce a slight increase of the continuum reflectance (by 7 %) and a slight decrease of the CO<sub>2</sub> signatures. They find however that compact polycrystalline CO<sub>2</sub> ice becomes brighter as it sublimates, probably as a result of surface scattering at the ice/gas interfaces of the joints boundaries as the ice becomes more porous. This mechanism is hypothesised to explain the brightening of the Martian seasonal polar caps observed in late Spring.

Finally, Portyankina et al. [55] simulated atmospheric conditions of pres-

sure and temperature close to the Martian ones and condensed atmospheric CO<sub>2</sub> on both metallic and dusty surfaces. They assessed the way in which the CO<sub>2</sub> condensed (e.g. flakes or slab), and confirmed the possibility of CO<sub>2</sub> to form centimeters-thick, highly translucent slabs of ice depending on the conditions of temperature and pressure.

### *1.6. Need for additional reflectance measurements*

While the spectra published more than 50 years ago by Kieffer [48, 49] are of excellent quality and with sufficient spectral resolution at wavelengths larger than 1.6  $\mu\text{m}$ , the shorter wavelength near-infrared is only covered with a few spectral bands and the visible range was not measured. The spectra were also normalised to 1, providing no information of the absolute reflectance level. The first objective of this work is to extend the spectral range for similar samples over the entire visible (0.4-1.0  $\mu\text{m}$ ) and near-infrared (1-2.5  $\mu\text{m}$ ) spectral ranges with high signal to noise and spectral resolution and sampling. Another main objective is to broaden the variety of solid CO<sub>2</sub> samples available for reflectance studies. In addition to CO<sub>2</sub> slabs, we introduce ways of producing granulated CO<sub>2</sub> ice samples, which are key to address the range of grain sizes observed on the Martian surface. We present a study of the reflectance of CO<sub>2</sub> ice, both pure and intimately mixed with water ice or JSC Mars-1. We also produced ternary mixtures of CO<sub>2</sub> ice, H<sub>2</sub>O ice and JSC Mars-1, and monitored their reflectance as the ices sublimated.

Our range of analogues necessarily includes idealised and simplified associations of ices and dust such as homogeneous intimate mixtures of the CO<sub>2</sub>/H<sub>2</sub>O ices and dust. It is unlikely that any process on Mars will produce –at a large scale– very homogeneous mixtures but such well-controlled

samples are ideal playgrounds for testing reflectance models. More complex samples are useful too and allow for more direct comparisons with the remote-sensing data but parameters are more difficult to control and the comparison with models is more challenging.

We discuss lessons learnt and remaining challenges to produce these samples. We then study strategic spectral criteria to characterise the results of our experiments, and propose methods to fully exploit our reflectance spectra. The spectra are also available in public databases for further/different analyses by interested readers. This paper is the continuation of the work published in Yoldi et al. [56], which provided laboratory data and spectral analysis to help interpret water ice and soil reflectance spectra from the Martian surface. Toward the end of the Result and Discussion Sections, we consider all results from the two articles to provide insights to interpret remote-sensing colour and spectral information in terms of the composition and physical properties of Martian icy surfaces.

## 2. Samples, instruments and methods

### 2.1. Samples

#### 2.1.1. Ices

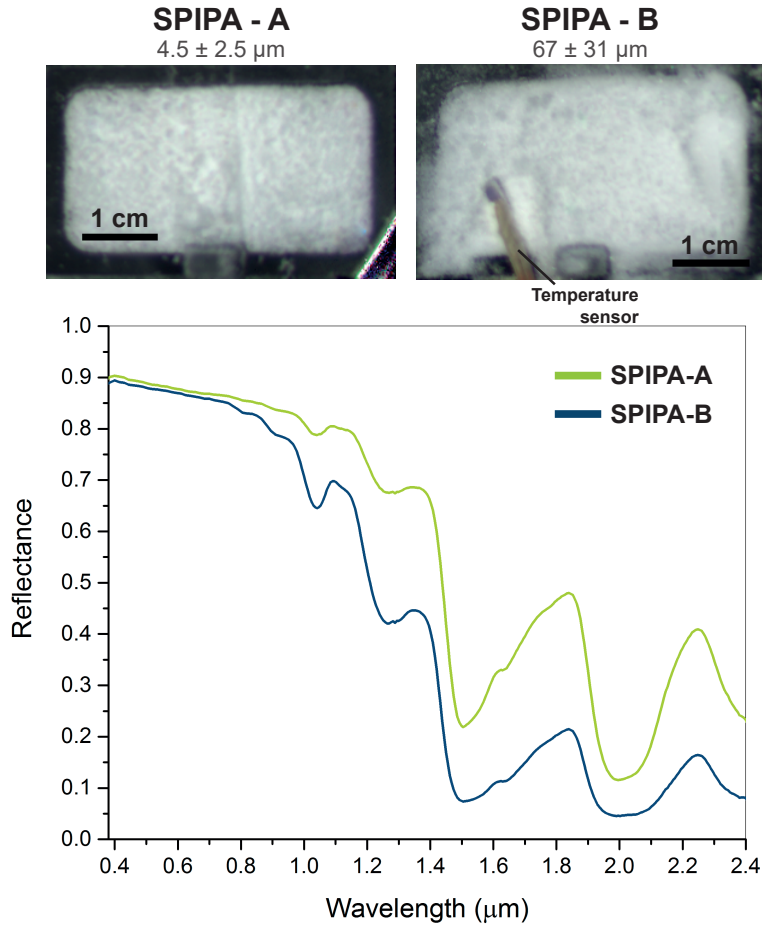


Figure 1: Top: Samples of fine-grained ( $4.5 \mu\text{m}$ , SPIPA-A)  $\text{H}_2\text{O}$  (left) and coarser grained ( $67 \mu\text{m}$ , SPIPA-B)  $\text{H}_2\text{O}$  (right) ices. Bottom: reflectance spectra of these two types of water ice.

$\text{H}_2\text{O}$  ice. We produced the granular water ice used in this study with the Setup for Production of Icy Planetary Analogues (SPIPA), at the Laboratory for Outflow Studies of Sublimating Materials (LOSSy) at the University

of Bern. In this study, we work with fine-grained ice (mean diameter:  $4.5 \pm 2.5$   $\mu\text{m}$ ) and coarser-grained ice ( $67 \pm 31$   $\mu\text{m}$ ), which we refer to as SPIPA-A and SPIPA-B respectively. Both SPIPA ices were produced by freezing nebulised, deionised water. We obtained different size distributions by using two different systems to nebulise the water. A detailed description of the production and characterisation of the SPIPA ices is available in Pommerol et al. [57]. Fig 1 shows pictures of the SPIPA samples, as well as their reflectance spectra.

We also caused atmospheric water to condense onto a slab of  $\text{CO}_2$  ice by exposing the slab to the atmosphere, outdoors, on a day with 93% of relative atmospheric humidity. Water frost did not condense homogeneously on the slab, which allowed us to study the spectra of different water frost thicknesses.

*CO<sub>2</sub> ice.* From frost [58] to thick and transparent slabs [59],  $\text{CO}_2$  ice is found in a variety of particle sizes on the Martian surface. In this study, we have used three types of pure  $\text{CO}_2$  ice, which we call  $\text{CO}_2$  frost,  $\text{CO}_2$  slab and crushed  $\text{CO}_2$  (Fig 2). We detail below the process of production of each one of these samples.

$\text{CO}_2$  frost was formed upon adiabatic cooling from pressurised  $\text{CO}_2$  gas using a commercial  $\text{CO}_2$  dry ice maker (Bel-Art<sup>TM</sup> SP Scienceware<sup>TM</sup> Frigimat<sup>TM</sup> Junior Dry Ice Make) and immediately stored in liquid nitrogen. Fig 2c shows a representative microscope image of the  $\text{CO}_2$  frost, from which we estimate the diameters of the individual  $\text{CO}_2$  grains to range between about 10  $\mu\text{m}$  and 100  $\mu\text{m}$  upon formation. The individual grains show a tendency to sinter as they form. Smooth necks joining the grains are clearly visible

under the microscope, which results in agglomerates of a few hundreds of micrometres. Unfortunately, the rapid sublimation of such fine grains of CO<sub>2</sub> at atmospheric pressure hampered further characterisation of these samples.

We have also used commercial CO<sub>2</sub> ice pellets purchased from Carbagas AG (1.4 kg slices, Reference: I5891XXX) and delivered in wedge-shaped ingots of few centimetres of maximal thickness. The ice is compact and translucent but not transparent. Internal fractures and joints are visible and scatter the light internally (2a). Note that the bare black rims of the sample holder cannot be distinguished from the frost-covered white surface through the cm-thick slab ice. We refer to these pellets as slab CO<sub>2</sub> ice hereafter. We broke the slabs into small pieces to place them in the sample holder, as can be seen in Figure 2a. We crushed some of the slabs and dry-sieved the resulting powder to obtain samples of CO<sub>2</sub> ice with various size distributions. We prepared three size distributions (Fig 2a): particles between 400 and 800  $\mu\text{m}$ , particles between 200 and 400  $\mu\text{m}$  and particles smaller than 200  $\mu\text{m}$ . Fig 2b shows an optical microscope picture of the fraction between 400 and 800  $\mu\text{m}$ . Unlike CO<sub>2</sub> frost, the crushed particles appear angular to sub-rounded because of the crushing process. Note also the fine-scale surface texture and the presence of internal fractures, pores or other types of defects within some of the particles (lower right corner) which effectively scatter the light

### *2.1.2. Martian analogues*

As a Martian soil analogue, we have used the Martian regolith simulant JSC Mars-1 [61], distributed by the Johnson Space Center. We already used this simulant in the first paper of this series [56].

For part of this study, we have used the JSC Mars-1 as distributed; all

the specifications regarding particle sizes, density, etc. are provided in Allen et al. [61]. We have also dry-sieved some of the original JSC Mars-1 to retrieve grains smaller than 100  $\mu\text{m}$ , which we used for the ternary mixtures. A Scanning Electron Microscope (SEM) picture of the fine grains and the reflectance spectra of both the original and the fine distributions are shown in Fig 3. Note that the size of the the fine Martian aeolian dust is estimated to be  $\sim 2 \mu\text{m}$  [62, 63] and while our fine fraction contains such very fine particles in large number, its mass distribution is dominated by the largest ones. In some contexts however, a broader size distribution is preferable. For instance, the jet activity observed over the cryptic region in the southern hemisphere and over dune fields in both hemispheres is known to mobilize and erode the Martian soil, depositing particles of all sizes over the seasonal ice.

### *2.1.3. Mixtures*

Here, we explain the methodology followed to create the mixtures used in this study. Table 1 provides an overview of the parameters and specifications of the samples.

*Binary mixtures.* We have developed and validated protocols to create intimate mixtures of water ice and refractory materials [57]. These protocols standardise the mixture production to guarantee the homogeneity and reproducibility of the samples. In short, we blend the ice and refractory materials with the help of a vortex shaker, alternating shaking and cooling intervals, during which we plunge the container with the samples into  $\text{LN}_2$ . The duration of these intervals is stipulated in the protocols.

We have adapted those protocols to produce CO<sub>2</sub> icy samples. The main difficulty of the process is the different sublimation points of H<sub>2</sub>O (273 K) and CO<sub>2</sub> (195 K) at 1 atm. To keep our working temperatures to a minimum, we kept the samples in aluminium bottles, which we plunged in LN<sub>2</sub>. We took the bottles out of the nitrogen to weigh and mix the materials in intervals of maximum 15 seconds. We also kept the sample holders (2x4x2 cm) into LN<sub>2</sub> until filled with the samples, and the cylinder that contained the sample holder was filled with LN<sub>2</sub>, as previously explained. The sample holders were filled inside a freezer to prevent water frost deposition.

We prepared the following intimate mixtures:

1. CO<sub>2</sub>-H<sub>2</sub>O: we mixed both crushed CO<sub>2</sub> and CO<sub>2</sub> frost with both fine grained and coarser grained H<sub>2</sub>O ice. We worked with small water weight percentages (10, 5 and 3 wt%) since it has already been shown that the water signature dominates the reflectance spectra from small quantities [49, 19]. Fig 4a shows intimate mixtures of CO<sub>2</sub> frost (10-100  $\mu$ m) and fine grained H<sub>2</sub>O ice ( $\sim$  4  $\mu$ m). Fig 4b shows intimate mixtures of crushed CO<sub>2</sub> and coarser grained H<sub>2</sub>O ice.
2. CO<sub>2</sub>-JSC Mars-1 intimate mixtures: by partitioning the sample holder, we obtained small volumes (2x2x2 cm) for multiple samples (Fig 4d). This way, we managed to measure several samples under the same conditions. JSC Mars-1 was mixed with 75, 50, 35, 10 and 5 wt% of crushed-CO<sub>2</sub>.

Even though the materials were homogeneously mixed, the reproducibility of the intimate mixtures of H<sub>2</sub>O and CO<sub>2</sub> can be improved. For example,

we observed the formation of pebble-like agglomerates for distinct grain sizes and water ice contents. Mixing materials in such ratios is challenging; the accuracy of water ice concentrations lower than 5 wt% is limited.

We also cannot exclude vertical variability within our samples. Either because of vertical segregation of particle sizes as we fill the holders with the particulate samples or as a result of thermo-physical evolutions of the samples (through sublimation, sintering...). Unfortunately, we have no means of assessing if vertical gradients of samples properties exist and their amplitude.

*Ternary mixtures.* We have developed a new methodology to create homogeneous mixtures of dust, CO<sub>2</sub> frost and H<sub>2</sub>O ice. These ternary mixtures will eventually be useful to simulate the volatile sublimation sequence observed during the retreat of the northern seasonal polar cap of Mars [30, 42, 45]. For these mixtures, we used the fine fraction of JSC Mars-1 (<100 μm) to simulate the dust grains suspended in the atmosphere that get trapped within the ice as CO<sub>2</sub> and H<sub>2</sub>O condense.

Figure 5 illustrates the process of production of the ternary mixtures. First, we produce the CO<sub>2</sub> frost, weigh it and immediately plunge it into LN<sub>2</sub>. We produce the H<sub>2</sub>O ice, and add it to the LN<sub>2</sub> and CO<sub>2</sub> mixture. We then add the dust to the mixture. At this point, the mixture looks as shown in Fig 5a. Table 1 shows the mass percentages used in each case.

When the LN<sub>2</sub> has evaporated enough that the liquid surface is below the top of the powder, the mixture presents a texture similar to that of plaster. We stir softly but constantly to mix the components of the mixture while the remaining nitrogen evaporates. Once the LN<sub>2</sub> has evaporated entirely, the mix solidifies (Fig 5b). Visual inspection confirms that the dust grains are

homogeneously distributed within the ice. Further stirring resulted in the loosening of the sample, whereas the non-manipulated sample would tend to compact as the CO<sub>2</sub> particles -in our case, the main component- sintered.

We present two different textures of the ternary mixtures: a powder-like one and a compressed one. The density of the samples was  $\rho_{fineH_2O} = 0.47 \text{ g/cm}^3$  and  $\rho_{coarserH_2O} = 0.488 \text{ g/cm}^3$  for the powdered samples and  $\rho_{fineH_2O} = 0.89 \text{ g/cm}^3$  and  $\rho_{coarserH_2O} = 0.846 \text{ g/cm}^3$  for the compacted ones. Fig 6a shows a microscope image of the powdered ternary mixture (with SPIPA-B). Seconds later, as CO<sub>2</sub> ice sublimated, the water particles became visible, as can be seen marked with red arrows in Fig 6b. Finally, Fig 6c shows the ternary mixture with SPIPA-B spread on a table; the sample on the left was spread on the table few minutes before the acquisition of the picture, and the sample on the right was spread right before acquiring the image. On the left, the carbon dioxide had completely sublimated, and only water ice and JSC Mars-1 is left.

Even though this protocol was effective to produce mixtures with both fine and coarser-grained H<sub>2</sub>O ice, we observed differences when using one or the other type of water ice. For example, the grains of the fine-grained water ice floated in liquid nitrogen forming aggregates, probably increasing the effective scatterer size of the water ice if they were not destroyed before solidification.

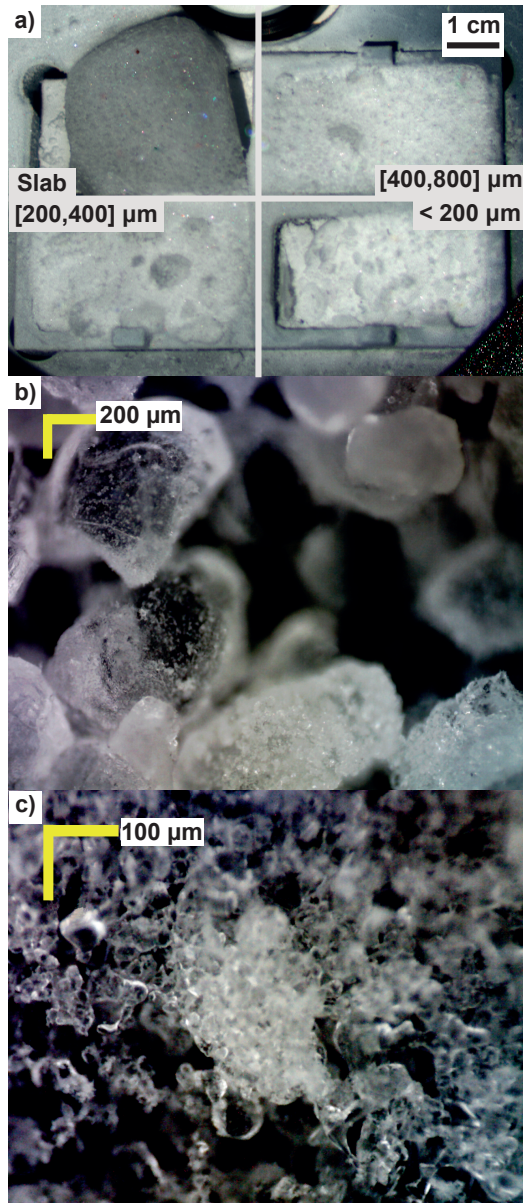


Figure 2: a) Three size fractions of crushed  $\text{CO}_2$  ( $400\text{-}800\ \mu\text{m}$ ,  $200\text{-}400\ \mu\text{m}$  and  $< 200\ \mu\text{m}$ ), along with a  $\text{CO}_2$  slab. These RGB images are exported from the hyperspectral cubes and appear slightly blurry due to the wide spectral range of the measurement. The resolution is  $\sim 50\ \mu\text{m}$ . b) Microscope image of the crushed  $\text{CO}_2$  ( $400\text{-}800\ \mu\text{m}$  fraction). c) Microscope image of the  $\text{CO}_2$  frost showing smooth and roundish particles with diameters ranging between  $10$  and  $100\ \mu\text{m}$ . Many of the particles show clear signs of sintering, being connected by small necks.

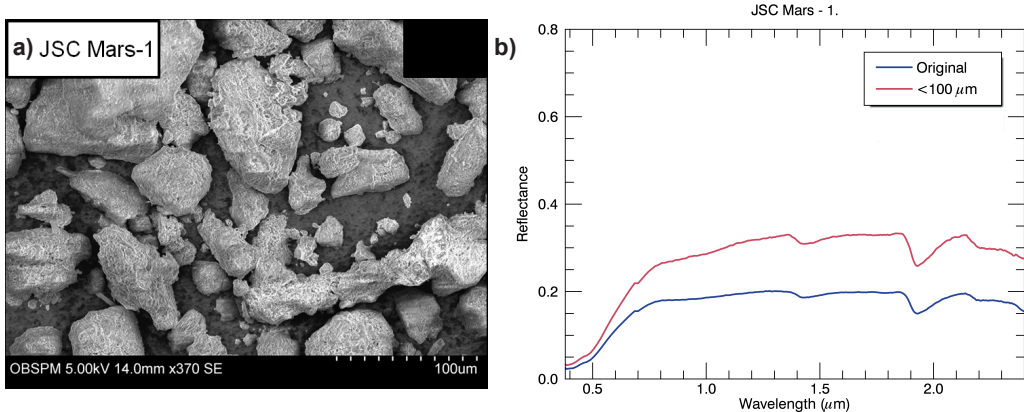


Figure 3: a) SEM picture of a sieved sample of JSC Mars-1 ( $<80 \mu\text{m}$ ). Picture extracted from Brouet [60]. b) Reflectance spectra of the original and sieved fraction ( $<100 \mu\text{m}$ ) of the JSC Mars-1

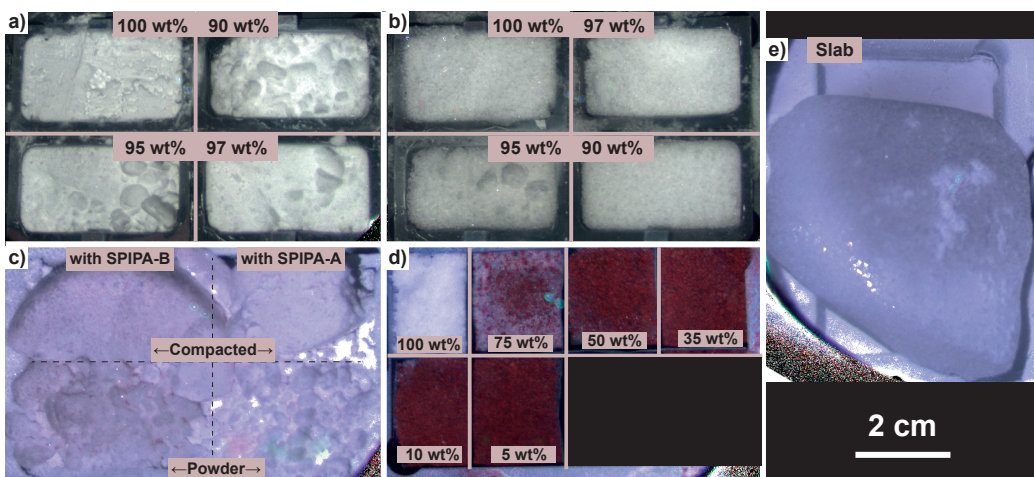


Figure 4: Mixtures with CO<sub>2</sub> ice. a) Various weight percentages of CO<sub>2</sub> frost (10-100  $\mu\text{m}$ ) intimately mixed with fine grained ( $\sim 4.5 \mu\text{m}$ ) water ice. b) Various weight percentages of crushed CO<sub>2</sub> (400-800  $\mu\text{m}$ ) intimately mixed with coarser grained ( $\sim 67 \mu\text{m}$ ) water ice. c) Ternary mixtures of CO<sub>2</sub>, fine grained H<sub>2</sub>O (right) or coarser grained H<sub>2</sub>O (left), and JSC Mars-1. On top, the mixtures have been compacted. d) Various weight percentages of crushed CO<sub>2</sub> (400-800  $\mu\text{m}$ ) intimately mixed with JSC Mars-1. e) Slab of compact CO<sub>2</sub> ice with some water frost (white) on the right side.

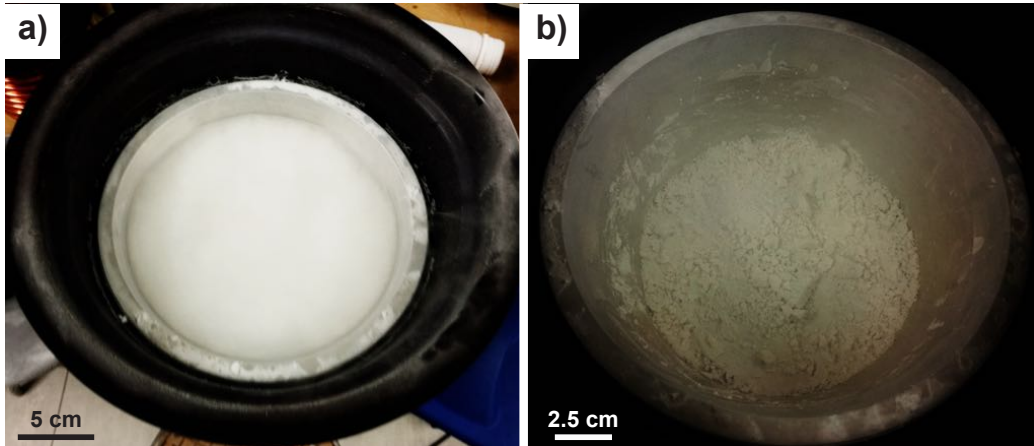


Figure 5: Two steps of the production of ternary mixtures. a)  $\text{CO}_2$  frost (10-100  $\mu\text{m}$ ), coarser grained  $\text{H}_2\text{O}$  ice ( $\sim 60 \mu\text{m}$ ) and JSC Mars-1 in liquid nitrogen. b) After sublimation of the liquid nitrogen, the components of the mixture settle down.



Figure 6: Sublimation of  $\text{CO}_2$  ice in the ternary mixtures. a) Microscope picture from the ternary mixture upon production. b) A few seconds afterwards, the first layer of  $\text{CO}_2$  has sublimated, revealing the SPIPA-B particles in the mixture (marked with red arrows). c) The ternary mixture left on a table for a few minutes (left) and freshly spread (right). The sample on the left has lost all the  $\text{CO}_2$  (whose initial contour is shown with the blue, dashed line), releasing the coarser  $\text{CO}_2$  ice grains and JSC Mars-1.

Mixing Mode	CO <sub>2</sub>	Size of CO <sub>2</sub> ice	Contaminant	Size of the Contaminant	Concentration of contaminant	T <sub>Shroud</sub> (K)	Duration of Measurements
—	Crushed	400-800 μm	—	—	—	128 K	1st scan: 30 mins Hyperspectral: 71 mins
Frost	Slab	Wedge shaped. Max dim: 8 x 5 x 2.8 cm	Water frost	Unknown.	From μm to ~mm-thick layer	160 K	1st scan: 30 mins Hyperspectral: 71 mins
Intimate mixture	Frost	Few μm. Agglomerates of hundreds of μm	SPIPA-A	4.5 ± 2.5 μm	3, 5, 10 wt%	148 K	1st scan: 30 mins Hyperspectral: 71 mins
			SPIPA-B	69 ± 31 μm		138 K	
	Crushed	400-800 μm	SPIPA-A	4.5 ± 2.5 μm	25, 50, 65, 90, 95 wt%	140 K	1st scan: 30 mins Hyperspectral: 71 mins
			SPIPA-B	69 ± 31 μm		150 K	
Ternary Intimate mixture	Frost	Few μm. Agglomerates of hundreds of μm	JSC Mars-1	71.7% > 150μm 28.3% < 150μm [61]	3 wt% 0.2 wt%	160 K	Total time: 11scans * 32 mins
			SPIPA-A	4.5 ± 2.5 μm			
	Frost	Agglomerates of hundreds of μm	JSC Mars-1	<100 μm	3 wt% 0.2 wt%	See Fig 7	Total time: 11scans * 32 mins
			SPIPA-B	69 ± 31 μm			
JSC Mars-1	<100 μm	3 wt% 0.2 wt%	See Fig 7	See Fig 7	See Fig 7	Total time: 11scans * 32 mins	

Table 1: Summary of the compositions, concentrations, mixture types and acquisition conditions of the experiments reported in this study.

## 2.2. Instrument description

We have acquired the reflectance data presented in this study with the Simulation Chamber for Imaging Temporal Evolution of Analogous Samples (SCITEAS) at LOSSy, the Laboratory for Outflow Studies of Sublimating icy materials of the University of Bern. SCITEAS is a vacuum and cold chamber monitored with an imaging system that allows us to characterise ice-bearing samples. Pommerol et al. [64] first described SCITEAS in 2015. In the first paper of this series [56], we have detailed improvements to the system. Further details, together with a list of the published studies carried out with SCITEAS can be found in Pommerol et al. [57]. Therefore, we only provide here the main characteristics of the instrument:

- Acquisition of hyper/multispectral cubes between 0.38 and 2.5  $\mu\text{m}$ .
- Samples can be kept at low temperature (down to 100 K) by flowing liquid nitrogen ( $\text{LN}_2$ ) through a cold shroud that surrounds the sample holder.
- The pressure can be reduced down to  $10^{-6}$  mbar.
- The spectral sampling is defined by the user. For hyperspectral acquisitions, we typically work with a sampling of 15 nm in the visible (VIS, 0.4-0.95  $\mu\text{m}$ ) and of 6 nm in the near-infrared (NIR, 0.95- 2.500  $\mu\text{m}$ ).
- The geometrical configuration of the instrument is set by default so that the incidence angle is around  $20^\circ$ , the emission angle is  $30^\circ$  and the phase angles are  $50^\circ$  in the visible and  $10^\circ$  in the near-infrared [64].

- The samples holder are made of aluminum and covered by a layer of black aluminum tape which has a constant reflectance of 0.05 over the entire spectral range investigated here. The holders are rectangular with LxWxH dimensions of 4x2x2cm.

At the time these experiments were conducted, the vacuum pumps of SCITEAS could not pump the CO<sub>2</sub> out of the chamber at a rate that would avoid building up pressure inside of it. The chamber was also not equipped with a cold plate below the sample. Both features were added later as a revised version of the chamber (SCITEAS-2) was built [65]. For safety reasons, we did not close the lid of the chamber completely when working with CO<sub>2</sub> ice to let the gas produced by sublimation escape from the chamber.

Performing the experiments under the laboratory atmosphere is of course different from the Martian conditions. There are two aspects to consider: First, the absolute pressure is higher by a factor of  $\sim 100$  and second the sublimation of CO<sub>2</sub> in the laboratory takes place in an inert atmosphere of nitrogen and oxygen with only traces of CO<sub>2</sub> while on Mars there is an equilibrium between a CO<sub>2</sub> ice surface and a CO<sub>2</sub> atmosphere. As a result of the absolute difference of pressure, sublimation in the lab will also occur at a higher temperature (195K vs. 140K), following the Clausius–Clapeyron relation. This will not affect the behaviour of water which is always far below its sublimation temperature in both cases. Higher pressure can also increase the vertical heat transport within the sample through gas conduction and convection, which in turn could have consequences for the metamorphism of the sample at various depths. Sublimating CO<sub>2</sub> ice in an inert gas atmosphere rather than in equilibrium with its pure gas phase is also likely to change

the outcome of the sublimation by affecting the sublimation speed and possible vertical transport and recondensation of CO<sub>2</sub> within the porosity of the sample [66]. Future work will ideally attempt to perform these sublimation experiments in conditions closer to the Martian surface and find out if the possible differences discussed here are indeed significant. Note that the influence of lab pressure is not only relevant for the sublimation but also for the growth. For example, [48] suggest that for a process limited by diffusion, the size of the frost crystals is proportional to the relative concentration of the condensable gas. Consequently, we can expect the Martian crystals of frost to be smaller than the ones grown in the laboratory. The effect of pressure (and temperature) on the morphology of crystals grown was studied experimentally by Portyankina et al. [55].

### *2.2.1. Acquisition time*

The acquisition of a hyperspectral cube under the current setting lasts 70 min [56]. However, CO<sub>2</sub> sublimates faster than that at the range of temperatures and pressures we work with. We have modified that spectral sampling to reduce the duration of the measurements: even though we keep the 6 nm sampling around absorption features in the NIR, we measure the reflectance only at specific wavelengths in the continuum. This acquisition mode lasts 30 min and will be referred to as *quick scan*.

Most of our measurements consist of a first, quick scan followed by a complete one. The second scan provides us with the entire shape of the spectra but with a larger CO<sub>2</sub> grain size due to sintering and/or reduced concentration of the finest grains of CO<sub>2</sub> due to sublimation. To monitor the sublimation of ices in the ternary mixtures at high temporal resolution, we

have used only quick scans.

### *2.2.2. Sublimation of ice from the samples*

At a constant pressure (i.e. 1 atm) and for a given grain size, temperature controls the sublimation of our ices. Table 1 shows the mean temperature measured on the shroud for each experiment. To reach such low temperatures at 1 atm, we filled the cylinder containing the sample holder (see Fig 2 in Pommerol et al. [64]) with LN<sub>2</sub> at the beginning of the experiment.

The evolution of temperature measured in the shroud and the air near the ternary mixtures is shown in Figure 7, where we have also marked the times at which each measurement (12 in total) started. The steep increase of temperature observed at t=140 min was intentional to speed up sublimation.

### *2.2.3. Water frost condensation on the samples*

As mentioned before, we were not able to seal the cold chamber during the experiments. However, the constant and intense out-gassing of the LN<sub>2</sub> from the sample holder keeps the chamber very dry, as nitrogen pushes the air out of the compartment. This keeps water frost deposition to a minimum, but does not completely avoid it.

To assess the amount of water cold trapped onto our samples, we added a control sample of pure CO<sub>2</sub> ice in each set of experiments. The H<sub>2</sub>O index at 1.5 μm (see Section 2.3.2) of the control samples allows us to assess the water frost trapped by the samples. While we do not have any way to directly assess the quantity of frost deposited, we can use empirical relations derived from previous work to estimate the frost thickness from the strength of the water absorption bands. In our previous work [56], we had used the 2-μm

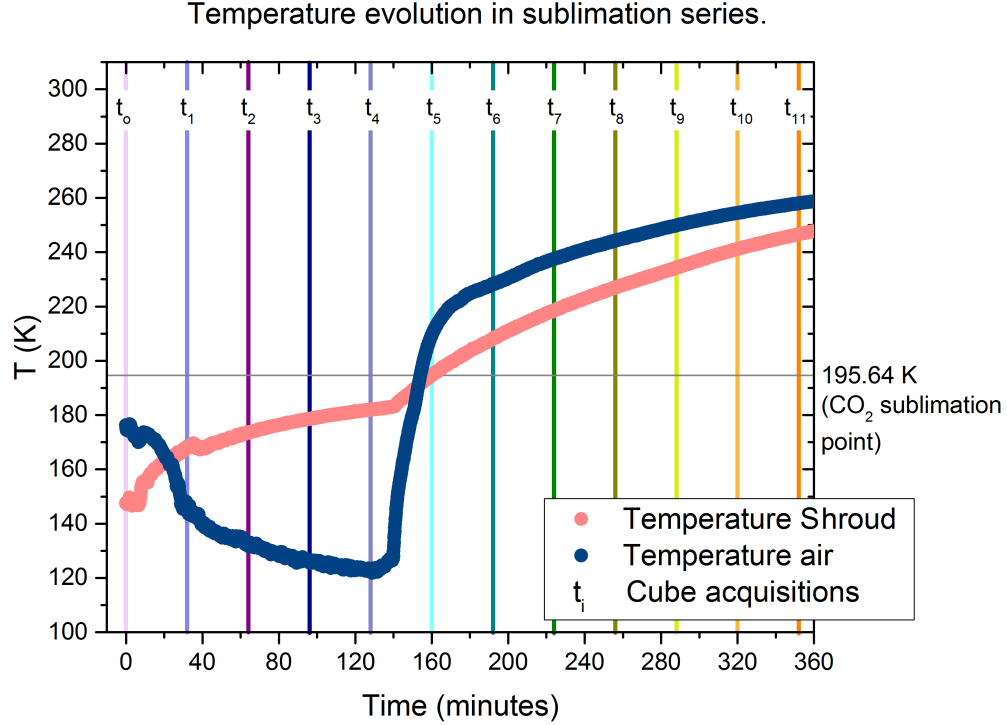


Figure 7: Evolution of the temperature of the shroud and the air at the surface surrounding the samples. The vertical lines indicate the time of acquisition of each of the 12 quick scans performed during the experiment. The horizontal line indicates the sublimation temperature of  $\text{CO}_2$  at atmospheric pressure.

band of  $\text{H}_2\text{O}$  for this purpose and an empirical relation derived from the data published by Clark and Lucey [67]. Here, we cannot use the 2- $\mu\text{m}$  absorption band of water because of the strong overlapping absorption of  $\text{CO}_2$  but the 1.5- $\mu\text{m}$   $\text{H}_2\text{O}$  band does not suffer from this problem. Digitizing the data from Clark and Lucey [67] for water frost grown over a Mauna Kea dust sample, we find a logarithmic relationship between the 1.5- $\mu\text{m}$  band depth and the frost thickness. Digitizing as well the two spectra from Kieffer [48] for  $\text{H}_2\text{O}$  frost grown over  $\text{CO}_2$  (same as in our work) and assuming a typical

porosity of 90 % [68], we notice that these two points fall over the same trend. This trend allows us to roughly estimate the frost thicknesses mentioned in the following sections, which vary between 25 and 400  $\mu\text{m}$  depending on the sample and the duration of the exposure to moist air. While the consistency between the results of [48] and Clark and Lucey [67] gives us confidence that these estimates are credible, an independent way to assess the thickness of the frost layer would be preferable and new developments are planned to allow such observations.

### *2.3. Data processing*

We convert the raw data into reflectance factor (REFF) units (as defined by Hapke [18]) through a calibration process detailed in Pommerol et al. [64]. We provide here the main steps of that process:

1. Before the measurement of the actual samples, we perform similar measurements (same cameras settings, spectral ranges and sampling, sample position) with a large, nearly-Lambertian surface (Spectralon<sup>TM</sup> (Labsphere)) covering the field-of-view of the camera.
2. Regularly during the measurements of the spectral cubes, we close a shutter installed at the monochromator and acquire dark images with the exact same settings as the actual images.
3. We interpolate temporally the dark signal and subtract it from the corresponding cube.
4. We divide the dark-signal corrected data acquired from the actual sample by the dark-signal corrected data acquired with the Spectralon sur-

face.

The calibration procedure outputs a reflectance hyper/multispectral cube in which we define Regions of Interest (ROIs) to extract averaged reflectance spectra from the desired areas.

### 2.3.1. *Uncertainties*

We detail in the first paper of this series [56], the procedure that we follow to assess the uncertainties of our measurements. Therefore, we only present here the major points of the procedure.

- Our sample holders contain an additional calibration target whose reflectance is known (i.e. Spectralon<sup>T</sup>M from Labsphere). By tracking the variation of its reflectance throughout the measurements, we assess their precision and accuracy.
- The average precision on our calibration target is  $\pm 0.3\%$  in the VIS and  $2\%$  in the NIR. This translates into signal-to-noise ratios (SNRs) of 333 and 50, respectively.
- Let us assume the scenario in which the uncertainty in the precision is entirely due to photon noise. In that case, the uncertainty varies with the square root of the signal, that is, of the reflectance of the sample. Following this, the SNR drops to 95 in VIS (relative error of  $1\%$ ) and 16 in NIR (relative error of  $6\%$ ) for a sample with a reflectance of  $10\%$ .
- We do not work with individual pixels, but with ROIs formed by hundreds to thousands of pixels. Consequently, the SNRs of our measure-

ments increase in average to much higher values (several hundreds) limited by the readout noise of the cameras and dark noise.

- We assess the accuracy of our measurements by comparing the theoretical reflectance of the calibration target with our measurements. This comparison shows a variability of 6% with the visible camera and 3% with the near-infrared.

Even though accuracy limitations control our uncertainties, the SNR and absolute accuracy have different implications on our spectral analyses. We favour the use of relative spectral criteria, where ratios between wavelengths of the same spectra are computed (i.e., slopes and band depths). These relative criteria are not affected by the absolute accuracy that affects the reflectance at all wavelengths in the same way and are only influenced by the SNR.

### 2.3.2. *Spectral analysis*

We study the reflectance spectra of our samples through the reflectance of the continuum, the depth of the absorption bands, the spectral slopes and the CaSSIS colours. We have chosen these parameters because they have been repeatedly used in other spectrophotometric studies (e.g., [30, 42, 36, 69]). We build on some of their choices and definition of parameters because we want our data to be comparable with existing data sets.

*Reflectance in the continuum.* The reflectance of the continuum allows us to distinguish bright from dark materials at a specific wavelength. It depends on various variables such as the single scattering albedo of the material or

the size of grains. Both CO<sub>2</sub> and H<sub>2</sub>O ices are bright in the continuum, but other materials, such as salts, are also bright in the continuum [65]. We have measured the reflectance of the continuum at 0.940  $\mu\text{m}$ . Langevin et al. [30] used the reflectance at 1.08  $\mu\text{m}$  as a reference for the reflectance in the continuum, based on a compromise between OMEGA instrumental considerations and the scattering of aerosols in the Martian atmosphere [30]. The difference in reflectance between these wavelengths is negligible for the CO<sub>2</sub> and JSC Mars-1 since they show flat spectra in this region. It is not the case for water ice, which presents a blue slope in the near-IR, but the difference of reflectance between these two positions lies within the uncertainties of the instrument.

*Evaluation of band depths.* The presence and position of absorption bands are specific to the materials (composition and state of the matter), and their depth to the length of the optical path inside the material (linked to the size and/or the amount of material present). We have analysed the absorption signatures of carbon dioxide at 1.435 and 2.281  $\mu\text{m}$  and of water at 1.5  $\mu\text{m}$ . For every band, we have used the evaluators proposed by Langevin et al. [30]. It is not straightforward to assess the strength of the CO<sub>2</sub> signature at 1.435  $\mu\text{m}$ , since it lies close to a CO<sub>2</sub> atmospheric absorption (around 1.444  $\mu\text{m}$ ) and it overlaps with the short wavelength side of the water band at 1.5  $\mu\text{m}$  (which starts at 1.38  $\mu\text{m}$  [30]). To minimise the impact of these two features, Langevin et al. [30] defined an evaluator (Eq (1)) from the reflectance (RF) of the spectra at 1.429, 1.385 and 1.443  $\mu\text{m}$ , which, adapted to the sampling of SCITEAS resulted in 1.432, 1.39 and 1.444  $\mu\text{m}$  respectively.

$$R = \frac{RF(1.432\mu m)}{RF(1.39\mu m)^{0.5} \times RF(1.444\mu m)^{0.5}} \quad (1)$$

Then, Langevin et al. [30] found a relationship between R and the CO<sub>2</sub> strength computed from water-free spectra (Eq (2)).

$$CO_2(1.435\mu m) = 1.16(1 - R)^{0.92} \quad (2)$$

As warned in Langevin et al. [30], the spectral element at 1.444 μm lies in the absorption signature of CO<sub>2</sub>, therefore (1-R) underestimates the strength of the band.

We used Eq (3) and (4) below to evaluate the absorption features at 2.281 μm (CO<sub>2</sub>) and 1.5 μm (H<sub>2</sub>O) respectively. The values of the wavelengths are slightly changed from the original values to adapt SCITEAS sampling.

$$CO_2(2.281\mu m) = 1 - \frac{RF(2.29\mu m)}{RF(2.226\mu m)^{0.3} \times RF(2.314\mu m)^{0.7}} \quad (3)$$

$$H_2O(1.5\mu m) = 1 - \frac{RF(1.498\mu m)}{RF(1.390\mu m)^{0.7} \times RF(1.774\mu m)^{0.3}} \quad (4)$$

As the band depth is defined as a ratio of two values of reflectance, the uncertainty on the band depth is only affected by the SNR.

*Spectral slopes.* The spectral slopes indicate how reflectance depends on the wavelength. They give us an idea of the colour of the materials, and is useful to identify the way in which materials are mixed [56]. We have assessed the spectral slopes with Eq (5).  $\lambda_1$  and  $\lambda_2$  have been set to 0.445 and 0.745 μm in the visible and 1.1 and 1.7 μm in the near-infrared.  $RF_{\lambda_1}$  and  $RF_{\lambda_2}$  refer to the values of reflectance at  $\lambda_1$  and  $\lambda_2$  respectively.

$$S_r = \frac{RF_{\lambda_2} - RF_{\lambda_1}}{RF_{\lambda_1}(\lambda_2 - \lambda_1)} \times 10^4 \quad (\%/100nm) \quad (5)$$

As for the band depth calculation, the relative uncertainties are therefore only affected by the SNR.

Throughout this study, we use the terms red, blue and flat slopes. A spectrum (or a region of a spectrum) has a red slope when its reflectance increases towards longer - or red- wavelengths. Red slopes imply positive spectral slope values, measured in %/100 nm. A spectrum (or a region of a spectrum) has a blue slope when its reflectance increases towards shorter - or blue- wavelengths. Blue slopes imply negative spectral slope values. A spectrum (or a region of a spectrum) is flat when it shows a constant reflectance, or spectral slope values  $\sim 0$  %/100 nm.

*Colour composites.* In the majority of cases, we present the spectral criteria averaged per ROI. In some cases, however, we also show the spatial variation of these criteria by showing the values per pixel. For that, we can either produce monochromatic images where the signal represents a particular spectral criterion, or we can combine three spectral criteria in RGB composites. When choosing the latter, we stretch each channel separately to emphasise the colours. We indicate the stretching applied to each channel with each RGB composite.

### 2.3.3. Colour analysis

The Colour and Stereo Surface Imaging System (CaSSIS, [70]) is the visible imager of the Exomars Trace Gas orbiter (EM-TGO). It consists of a 4-mirrors telescope with a focal length of 880mm, a 2k x 2k pixels CMOS sensor

and a rotation mechanism to align the telescope and sensor with respect to the ground track and obtain nearly-simultaneous stereo images of the surface. On top of the CMOS sensor, four broadband bandpass filters are mounted to image the surface in four colours. The respective filter names, effective central wavelengths and bandwidths (in nm) are: BLU (494.8, 133.6), PAN (678.2, 231.9), RED (836.0, 98.5), and NIR (939.3, 121.8). Because of the non Sun-synchronous orbit of TGO and the high sensitivity of the instrument, CaSSIS is able to observe the surface at variable local Solar times throughout the seasons and collects a unique dataset to study the diurnal and seasonal Martian volatiles cycles.

The simulated CaSSIS colours inform us on the possibilities and limitations of the instrument when it comes to detecting and distinguishing CO<sub>2</sub> and H<sub>2</sub>O ices. It also provides us with prior knowledge to target the observations of the Martian surface. We have convolved the data measured with SCITEAS with the spectral response of the instrument [70]. This methodology is automatised in the calibration software of SCITEAS and was detailed in Yoldi et al. [56]. Briefly, it is a process in which we take into account (i) the illumination conditions at an average Sun-Mars distance and a simulated incidence angle, and (ii) the specificities of CaSSIS (angular aperture of the telescope, area and reflectivity of the mirror, quantum efficiency, transmission of the filters, etc.), to simulate the reflectance that would have been measured by CaSSIS from samples like ours.

To compute the parameters introduced so far (reflectance in the continuum, indices and spectral slopes), we need to know the reflectance of the samples at specific wavelengths. However, to simulate the CaSSIS colours,

we need to know the reflectance of the samples in the spectral intervals that correspond to each filter (BLU, PAN, RED or NIR). The more measurements we have in an interval, the more accurate our simulations are. That is why the CaSSIS colours are the only spectral parameter that we derive from hyperspectral measurements and therefore, they represent the samples when they have already undergone sintering and sublimation.

Note that the bandpass filters of CaSSIS were designed to be very close to those of HiRISE with the infrared filter of HiRISE (IR) split into the RED and NIR filters of CaSSIS to provide additional sensitivity to iron-bearing mineralogy. Therefore, nearly all observations valid for the CaSSIS filters are also relevant for HiRISE.

### 3. Results

#### 3.1. Pure CO<sub>2</sub> ice

Fig 8 shows the reflectance spectra and their byproducts for various size distributions of CO<sub>2</sub> ice. Fig 8a and Fig 8b evince that the reflectance of the samples is inversely proportional to the size of their grains. The differences in reflectance between Fig 8a and Fig 8b are due to the sintering and/or sublimation of the finest particles of CO<sub>2</sub> ice during the experiments. Fine grains are more affected by this morphological evolution. The slab shows relatively low reflectance ( $\sim 0.5$ ) in the continuum, which suggests that part of the photons crossed the slab and reached the black sample holder. Kieffer [49] reports that water frost causes reflectance to peak at 1.8 and 2.24  $\mu\text{m}$ ; we do observe variations around those wavelengths between the multi- and hyperspectral measurements in, for instance, the slab.

The strength of the water index at 1.5  $\mu\text{m}$  (Fig 8c) indicates that, exposed to the same conditions of relative humidity and temperature, the smallest particles ( $< 200 \mu\text{m}$ ) cold-trapped more water frost than larger size fractions. Granular ices present lower CO<sub>2</sub> indices than the slab as the path of the photons is longer in continuous media. Both CO<sub>2</sub> indices (at 1.435 and 2.281  $\mu\text{m}$ ) remain relatively constant (around 0.1 and 0, respectively) for the particulate samples.

The VIS and NIR spectral slopes are relatively flat (i.e., around 0 %/100 nm) for all the CO<sub>2</sub> samples (Fig 8d). The trapped water frost explains the small shift of particulate CO<sub>2</sub> ice towards blue slopes ( $\sim -1$  %/100 nm); it was shown in Yoldi et al. [56] that low amounts of water frost on samples suffice to lower their visible slopes to negative values. This particular spectral

behaviour was also already modeled by [71] and [19] with similar results.

Finally, we show in Fig 8e the simulated CaSSIS colours. Because we obtain the CaSSIS colours from the hyperspectral measurements, the samples have already evolved. For this reason, the CaSSIS colours do not show a large difference in reflectance between the fine and the coarse ice grains. We see no significant difference of reflectance between measurements within the different filters of CaSSIS.

### *3.2. CO<sub>2</sub> slab with water frost*

Fig 9 shows the reflectance spectra and their byproducts for three ROIs drawn on the CO<sub>2</sub> slab covered with water frost (Fig 9a). ROI #1 is the one with most water frost ( $\sim 400$   $\mu\text{m}$  thickness), and ROI #3 the one with the least ( $\sim 75$   $\mu\text{m}$  thickness). For comparison purposes, we have added the spectrum of the slab shown in Fig 8, on which we did not condense any water intentionally but is still slightly affected by water frost ( $\sim 25$   $\mu\text{m}$ ).

ROIs with more water frost condensed show high reflectance levels (Fig 9a and Fig 9b). Compared to the slab that had not been exposed to atmospheric water, ROI #3 shows slightly lower reflectance. We attribute this small variation to a putative difference in the roughness of the ice surface caused by the outdoor exposure of the CO<sub>2</sub> slab. Fig 9a and Fig 9b do not show great differences in the absolute reflectance levels, as slabs do not evolve during the experiments as much as small particles do.

The H<sub>2</sub>O indices at 1.5  $\mu\text{m}$  follow the amount of water frost in each ROI (Fig 9c). Both CO<sub>2</sub> indices are negatively correlated with water frost thickness, as fewer photons reach the CO<sub>2</sub> slab due to scattering by the fine-grained H<sub>2</sub>O frost at the surface. ROI #3 shows slightly higher indices than

the water frost-free slab, which can as well be explained by differences in the thickness of the slabs.

We see in Fig 9d that the VIS slope is slightly more sensitive to the amount of water frost condensed on the slabs than the NIR slope. The presence of water frost turns the visible spectral slope blue.

Measured with CaSSIS, the ROIs with water frost would appear up to 20% brighter than the non-contaminated slab (Fig 9e). Because of the blue slope induced by water frost, ROIs with more frost appear brighter in the BLU filter ( $\sim 400 - 550$  nm) than in the red ones (PAN:  $\sim 550 - 800$  nm; RED:  $\sim 800 - 900$  nm; RED:  $\sim 900 - 1100$  nm).

### 3.3. $CO_2$ and $H_2O$ ice intimate mixtures

Fig 10 shows the reflectance spectra of the  $CO_2$  (frost, crushed) and  $H_2O$  (fine, coarser) intimate mixtures. For all the different combinations, we see that the pure  $CO_2$  sample is not the brightest. This is the result of the difficulties of mixing  $CO_2$  ice with other components discussed previously.

We see that water ice affects the reflectance spectra of the mixtures out of proportion to its concentration; water concentrations as low as 3 wt% are enough to dominate the spectrum. We see different behaviours in the continuum and the absorptive regions of the spectra. The reflectance of the continuum and other weak absorption features of water seems to be controlled by the texture (grain size, shape, surface roughness, density...) of the samples, which are not homogeneous due to the formation of agglomerates (see Fig 4a). The reflectance in the spectral regions of the absorption bands of water (centred at 1.5 and 2.0  $\mu\text{m}$ ), however, is more sensitive to the composition of the samples.

Fig 11 shows the reflectance spectra of the CO<sub>2</sub> (frost, crushed) and H<sub>2</sub>O (fine, coarser) intimate mixtures. We have added the pure spectra of the fine and coarser grained H<sub>2</sub>O ices for comparison.

Overall, we observe that the samples with CO<sub>2</sub> frost (10-100 μm) sublime faster than those with crushed CO<sub>2</sub>. By the shape of the CO<sub>2</sub> absorption bands within that of water ice at 2.0 μm, we see that CO<sub>2</sub> ice resists sublimation better when mixed with coarser H<sub>2</sub>O ice particles than with finer ones.

Comparing Fig 10 and Fig 11, we see that samples with more water show a greater drop in the reflectance from the multi- to the hyperspectral figures. As CO<sub>2</sub> ice sublimates, the CO<sub>2</sub> - to - H<sub>2</sub>O decreases and water ice forms a lag that dominates the spectrum.

Fig 12 shows the CO<sub>2</sub> and H<sub>2</sub>O indices for intimate mixtures with CO<sub>2</sub> frost (Fig 12a) and crushed CO<sub>2</sub> (Fig 12b). The H<sub>2</sub>O indices of mixtures with 5 wt.% of water ice are already half of that of the same mixtures with 100 wt% of water ice.

The CO<sub>2</sub> indices decrease with the concentration of CO<sub>2</sub>. A reduction of 10 wt% of CO<sub>2</sub> ice within the mixtures reduces the index at 1.4 μm by ~38% for the samples with CO<sub>2</sub> frost and by ~33% for the samples with crushed CO<sub>2</sub>. The index at 2.281 μm is so weak that it cannot be measured in the majority of the cases.

We see that, in general, the VIS and NIR spectral slopes are bluer with increasing concentration of H<sub>2</sub>O ice in the mixture (Fig 13a and 13b).

As seen in Fig 10 and Fig 11, the visible part of the spectra is dominated by the texture of the samples rather than by their composition. Consequently,

the reflectance measured with CaSSIS (Fig 13c and 13e) does not overall follow the composition of the samples. As CO<sub>2</sub> ice covers water ice and the spectral slope becomes neutral, the different filters measure similar values of reflectance.

#### *3.4. Crushed CO<sub>2</sub> ice and JSC Mars-1 intimate mixtures*

Fig 14a and Fig 14b show that the reflectance of the intimate mixtures of JSC Mars-1 and crushed CO<sub>2</sub> drops as the amount of ice decreases. Compared to the spectra of crushed ice of same size distribution (Fig 8a, Fig 8 b), the pure CO<sub>2</sub> ice shown here is about 20% darker. This can be due to the broad size distribution that we are using (400-800  $\mu\text{m}$ ); if the histogram of grain size distribution peaks towards 800  $\mu\text{m}$ , then the reflectance is expected to be weaker than if it peaks towards 400  $\mu\text{m}$ . We also see that samples which initially contained up to 35 wt% of CO<sub>2</sub> ice only show a weak CO<sub>2</sub> absorption around 2.29  $\mu\text{m}$ . In the VIS, we can identify the red slope characteristic of JSC Mars-1 when the weight of dust is only a quarter of that of the sample.

We analyse in Fig 14c the CO<sub>2</sub> and H<sub>2</sub>O signatures of the samples. The spectrum of JSC Mars-1 shown here was not measured together with the rest of the samples, and therefore its H<sub>2</sub>O index reflects its degree of hydration. The water index shows no correlation between the cold-trapped water frost and the CO<sub>2</sub> wt%. Instead, we attribute the variation in cold-trapped water frost to the process of filling of the sample holders, which was longer than usual as there were more samples to fill. Both CO<sub>2</sub> signatures tend to increase with the weight percentage of CO<sub>2</sub>; as observed previously, the signature at 1.435  $\mu\text{m}$  is stronger than the one at 2.281  $\mu\text{m}$ .

Fig 14d shows that the VIS slope of the sample with 5 wt% of CO<sub>2</sub> ice is

reduced by a 50% compared to JSC Mars-1, and it continues decreasing as the percentage of carbon dioxide increases. In the NIR, the spectral slope remains flat-to-bluish, oscillating from 0 to -4 %/100 nm following the amount of water frost condensed at the surface of the samples.

Measured with CaSSIS (Fig 14e), the presence of JSC Mars-1 results in reflectance measurements in the BLU filter around 30% weaker than in other filters. This gap between the reflectance measured in the different filters narrows as the percentage of ice increases until it disappears entirely for the pure CO<sub>2</sub> sample. With 75wt% of CO<sub>2</sub> ice, the BLU filter still measures 20% lower reflectance than the other ones. This value is similar to the ones measured in [56] for water ice and JSC Mars-1 intimate mixtures.

### *3.5. Sublimation series of the ternary mixtures*

Fig 15 is a 2x2 matrix of plots showing the evolution of the reflectance spectra of the ternary mixtures as the CO<sub>2</sub> and H<sub>2</sub>O ices sublimated. The rows correspond to the size of water ice (fine or coarser) and the columns to the texture of the samples (compact or powder). The four samples initially had the same composition: 96.8 wt% of CO<sub>2</sub> frost, 3 wt% of water ice and 0.2 wt% of JSC Mars-1 ( particles smaller than 100 μm).

We observe similarities with the binary mixtures, namely: 1) A shape of the spectra dominated by water ice, even if present at low concentrations. 2) A first, relatively abrupt, darkening of the sample (between  $t_0$  and  $t_1$ ), explained by the quick sublimation of cold-trapped water frost. 3) A progressive change in the shape of the water bands towards broader and less complex bands, indicating the warming up of the samples. 4) The VIS (400-950nm) shows greater variation in these plots, since that region is more sensitive to

changes in the texture.

The compacted samples initially show a higher reflectance than the powdered ones, partly explained by the trapped water frost.

We observe a non-intuitive behaviour of the absorption band of CO<sub>2</sub> around 2  $\mu\text{m}$  in the samples with fine H<sub>2</sub>O ice, which does not seem to occur with coarser H<sub>2</sub>O ice. The band decreases to a minimum at  $t_3$  to later on grow again and be noticeable by the end of the experiment, when the temperature of the air above the sample was of 250 K (55 K above the sublimation point of CO<sub>2</sub> at atmospheric pressure (Fig 7)).

The evolution of carbon dioxide and water indices (Fig 16a) shows a growing H<sub>2</sub>O index at 1.5  $\mu\text{m}$  as CO<sub>2</sub> sublimates. For all the samples, there is an initial, steep increase of the water index, that slows down after  $t_3$ . As observed in Fig 15, the evolution of the CO<sub>2</sub> index depends on the size of the water ice. The CO<sub>2</sub> indices in samples with fine grained water ice decreases by around half from  $t_0$  to  $t_4$  and stay constant around 0.025 until  $t_9$ . The CO<sub>2</sub> indices in samples with coarser grained water ice oscillate around 0.075 from  $t_0$  to  $t_4$  and then decrease down to 0.05 until  $t_9$ . After that, the CO<sub>2</sub> indices of every sample start increasing until the end of the measurement. We do not detect any absorption at 2.281  $\mu\text{m}$  during the duration of the experiment.

Fig 16b shows the evolution of the visible and near-infrared spectral slopes of the ternary mixtures. The ternary mixtures are a combination of components with different spectral slopes; (i) CO<sub>2</sub> ice, with no slope in both the VIS and NIR ranges, (ii) H<sub>2</sub>O ice, with blue slopes in the visible ( $\sim -1\%/100$  nm) and near-infrared (SPIPA-A:  $-8.4\%/100$  nm, SPIPA-B:  $-13\%/100$  nm)

spectral ranges, and (iii) JSC Mars-1, red in the visible ( $\sim 140\%/100$  nm) and flat in the near-infrared range. Because of the neutral slopes of CO<sub>2</sub> ice, this component only impacts the reflectance slopes by how much it covers or uncovers the other components.

In the visible range of the spectrum, the slopes are expected to become redder as water ice sublimates and the relative abundance of JSC Mars-1 increases. The ternary mixtures with coarser grained water ice show such a behaviour, as a dust lag formed with the sublimating ice. The spectral slopes of ternary mixtures with fine grained H<sub>2</sub>O ice, however, remained constant around 2.5 %/100 nm during the six hours of the experiment; the scattering by small ice particles dominated the reflectance. We can assume that we would have seen the same dust lag after some additional hours of sublimation. In the same way, the NIR spectral slopes of these samples are dominated by water ice. Because there is no water absorption associated with the transient decrease in the spectral slope of the powdered sample with coarser grained water ice (see Fig 15a) at  $t_8$ , we assume this point to possibly be an instrumental artefact.

### *3.6. Comparison of criteria. Addition of water ice and dust experiments*

We compare now the criteria defined in Section 2 for all the experiments. We aim to find trends among the samples to eventually identify them in terms of composition and mixing mode. We used the same strategy in the first part of this study, where we focused on water ice and dust associations [56]. Hence, we have added to some of the plots the experiments with water ice and JSC Mars-1 conducted in Yoldi et al. [56]. We provide here a summary of the water ice experiments to ease reading of the figure. The corresponding

legend is given in Fig 17ii).

1. *JSCM-1 + Water frost samples*: experiments in which water frost was condensed onto various size fractions of JSC Mars-1. By sporadically exposing the samples to the atmosphere, we studied the reflectance of different thickness of water frost on the regolith.
2. *Intimate mixtures*: JSC Mars-1 and SPIPA-A or SPIPA-B mixtures. We mixed the original size distribution of JSC Mars-1 with 10, 35, 50 and 75 wt% of SPIPA-A and SPIPA-B separately.
3. *Frozen soils*: experiments in which we thoroughly wet various size fractions of JSC Mars-1 and froze them. The result was a matrix of water ice surrounding the JSC Mars-1 grains. We measured the reflectance of the samples as ice sublimated.

Fig 18a compares the reflectance of the continuum (0.940  $\mu\text{m}$ ) to the  $\text{CO}_2$  indices of the samples. For clarity, the X-axis only shows values up to 0.5. The pure ice samples (blue symbols) occupy reflectance values from  $\sim 1.0$  to 0.5 and  $\text{CO}_2$  indices between 0.1 and 0.3. JSC Mars-1 and crushed  $\text{CO}_2$  intimate mixtures group on the bottom left of the graph, with reflectance values and  $\text{CO}_2$  indices lower than 0.4 and 0.1 respectively. The ternary mixtures cover a large range of reflectance values and are grouped on the left side of the graph with  $\text{CO}_2$  indices lower than  $\sim 0.1$ .

We compare in Fig 18b the  $\text{CO}_2$  index and the VIS (top graph) and NIR (bottom) spectral slopes. The graph at the top is L-shaped. There is a vertical column around 0-values of the visible spectral slopes formed by pure ice samples. Samples with JSC Mars-1 fill the horizontal section of the graph

with CO<sub>2</sub> index values of 0.1 and a wide range of spectral slopes depending on their content of JSC Mars-1. For reference, the visible spectral slope of pure JSC Mars-1 exceeds 100%/100 nm. The graph on the bottom shows a shrunk, flipped L-shape. This plot differentiates intimate mixtures of CO<sub>2</sub> and H<sub>2</sub>O mixtures (around -3 and -7 %/100 nm) from pure CO<sub>2</sub> samples that trapped water frost (around 0 and -2 %/100 nm). Ternary mixtures show the bluest slope of all samples, ranging from -4 to almost -10 %/100 nm. Intimate mixtures of crushed CO<sub>2</sub> and JSC Mars-1 fall together with the pure CO<sub>2</sub> samples, except for the points that correspond to samples with more JSC Mars-1.

In Fig 18c, we compare the reflectance in the continuum and the H<sub>2</sub>O index at 1.5 μm. The experiments with CO<sub>2</sub> and hydrated minerals (JSC Mars-1), the granular CO<sub>2</sub> that trapped atmospheric water and the experiments where water frost had condensed on a CO<sub>2</sub> slab cluster to the left, below H<sub>2</sub>O indices of 0.2. The exception is the ROI on the slab that was completely covered by water frost, whose water index is ~0.25. As seen previously, this group of experiments presents a wide range of reflectance values, from ~1.0 for the finest CO<sub>2</sub> grains to 0.2 for the samples containing high amounts of JSC Mars-1. Intimate mixtures of CO<sub>2</sub> and H<sub>2</sub>O ice form a group above reflectance values of 0.7 and between H<sub>2</sub>O index of 0.2 and ~0.5. These points get progressively closer to the values of pure water ice. They do not, however, follow a linear path since -as seen previously- the reflectance spectra in the visible is more dependent on the texture of the sample than on the CO<sub>2</sub>-to-H<sub>2</sub>O ratio. Finally, ternary mixtures are seen at high values of H<sub>2</sub>O indices (0.4-0.8) and spread reflectance values (0.25-1.0).

In Fig 18d, we incorporate the water ice and JSC Mars-1 samples from Yoldi et al. [56]. CO<sub>2</sub> and JSC Mars-1 intimate mixtures cluster together with the JSC Mars-1 samples on which water frost condensed, which indicates that intimate mixtures trapped atmospheric water. Fig 18d also evinces that CO<sub>2</sub> ice (non-absorptive material) intimately mixed with only a 3 wt% of water ice shows water indices as strong as JSC Mars-1 (absorptive material) intimately mixed with 35 wt% of water ice. We also note that as the loose ternary mixtures sublime, they join the points representing the intimate mixtures of water ice and JSC Mars-1.

In the top graph of Fig 19e, we compare the water index at 1.5  $\mu\text{m}$  with the VIS spectral slope. The distribution of the points is similar to that observed in Fig 18b. Here, however, the ternary mixtures are easily distinguishable from the JSC Mars-1 and CO<sub>2</sub> ice intimate mixtures, since they show high H<sub>2</sub>O indices (0.4 to 0.7 compared to a maximum of 0.2 for the mixtures without water ice). This graph also distinguishes between CO<sub>2</sub> samples that trapped small quantities of atmospheric water and intimate mixtures of CO<sub>2</sub> and H<sub>2</sub>O ices. The graph on the bottom compares the water index to the NIR spectral slope: all the samples follow a similar path from flat slopes towards the slope values of pure water ice.

When we add the water experiments (Fig 19f), we see that, for the VIS, most of the water experiments fill in the gap left by the L-shaped graph drawn by the CO<sub>2</sub> samples. The JSCM-1/water frost experiments overlap again the CO<sub>2</sub> and JSC Mars-1 intimate mixtures. Looking at the NIR spectral slopes, the JSC Mars-1 and water frozen soils fall outside the trend drawn by the CO<sub>2</sub> experiments.

Finally, we compare in Fig 19g the reflectance measured in the RED filter of CaSSIS to the PAN/RED and BLU/RED filter ratios. We have zoomed into the X-axis of the PAN/RED band ratio. We do not include in these graphs the ternary mixtures since we only performed quick scans with those samples, which does not allow us to perform CaSSIS colour simulations (see Section 2). Both graphs allow us to separate the samples bearing JSC Mars-1 from those of pure ice. All the pure ice samples gather around band ratios of 1, samples with pure water being redder than the ones with CO<sub>2</sub>. When we add the water ice samples to the plot (Fig 19h), CO<sub>2</sub> and JSC Mars-1 intimate mixtures do not align with the water ice and JSC Mars-1 intimate mixtures. Instead, intimate mixtures of CO<sub>2</sub> and JSC Mars-1 fall in between the intimate mixtures of water ice and JSC Mars-1 and the frozen soils. This is because CO<sub>2</sub> ice has a redder spectral slope than water ice. Hence, the intimate mixtures with CO<sub>2</sub> and JSC Mars-1 plot below and parallel to the intimate mixtures with H<sub>2</sub>O ice and JSC Mars-1.

## CO<sub>2</sub> ice.

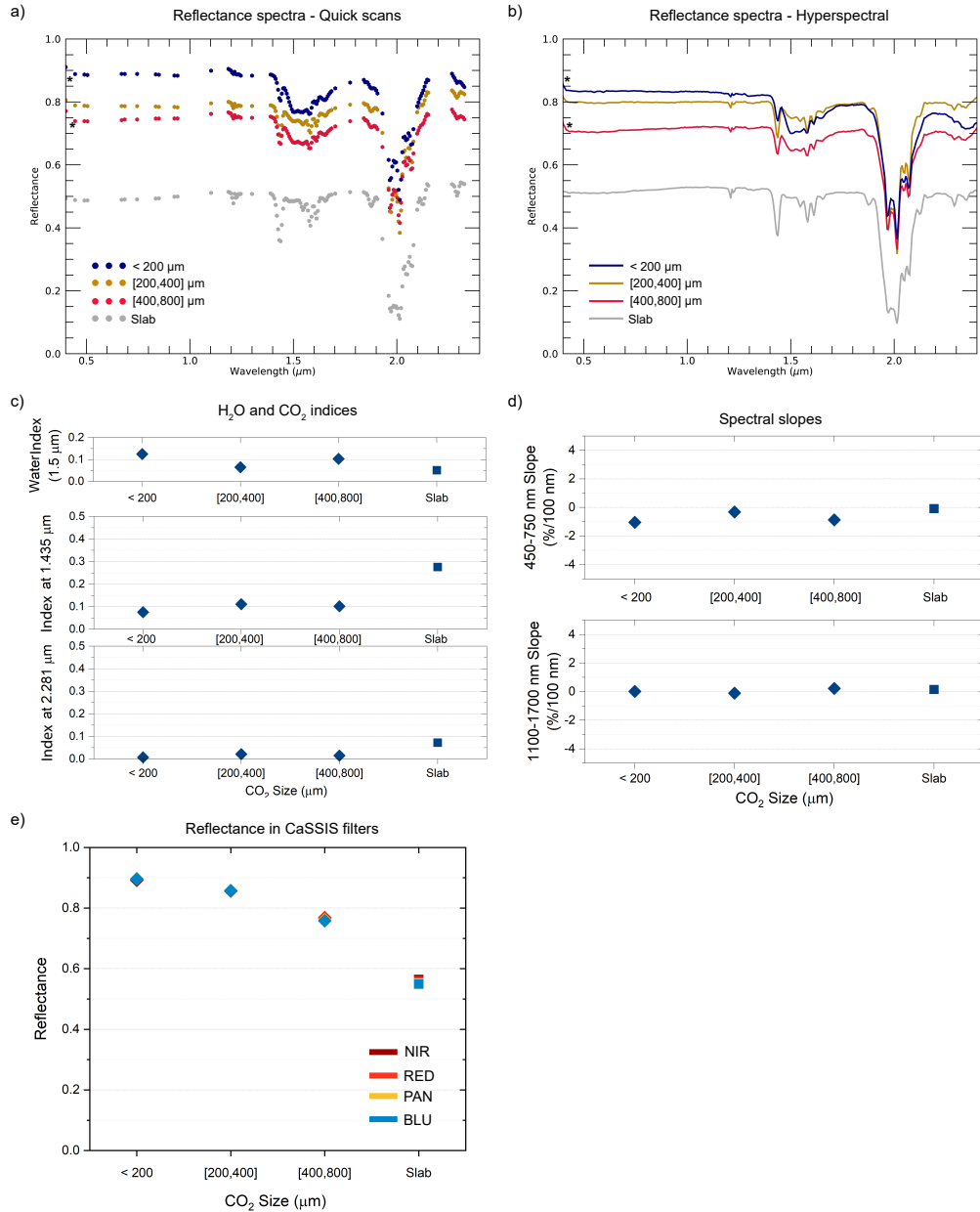


Figure 8: a) Multispectral reflectance spectra for various CO<sub>2</sub> grain sizes. b) Hyperspectral reflectance spectra for various CO<sub>2</sub> grain sizes. c) Strength of various absorption features: the one from H<sub>2</sub>O at 1.5 μm (indicative of the cold-trapped water) and the ones at 1.435 and 2.281 μm of CO<sub>2</sub> ice. d) VIS and NIR spectral slopes of the samples. e) Simulated reflectance measured in the CaSSIS filters. \* Stars indicate calibration artifacts at the shortest wavelengths. All CO<sub>2</sub> samples appear contaminated by H<sub>2</sub>O frost with estimated thicknesses of 100 μm, 50 μm, 75 μm and 25 μm (from the finest to the coarsest size fraction) based on the strength of the 1.5 μm feature.

### Water frost over CO<sub>2</sub> slab.

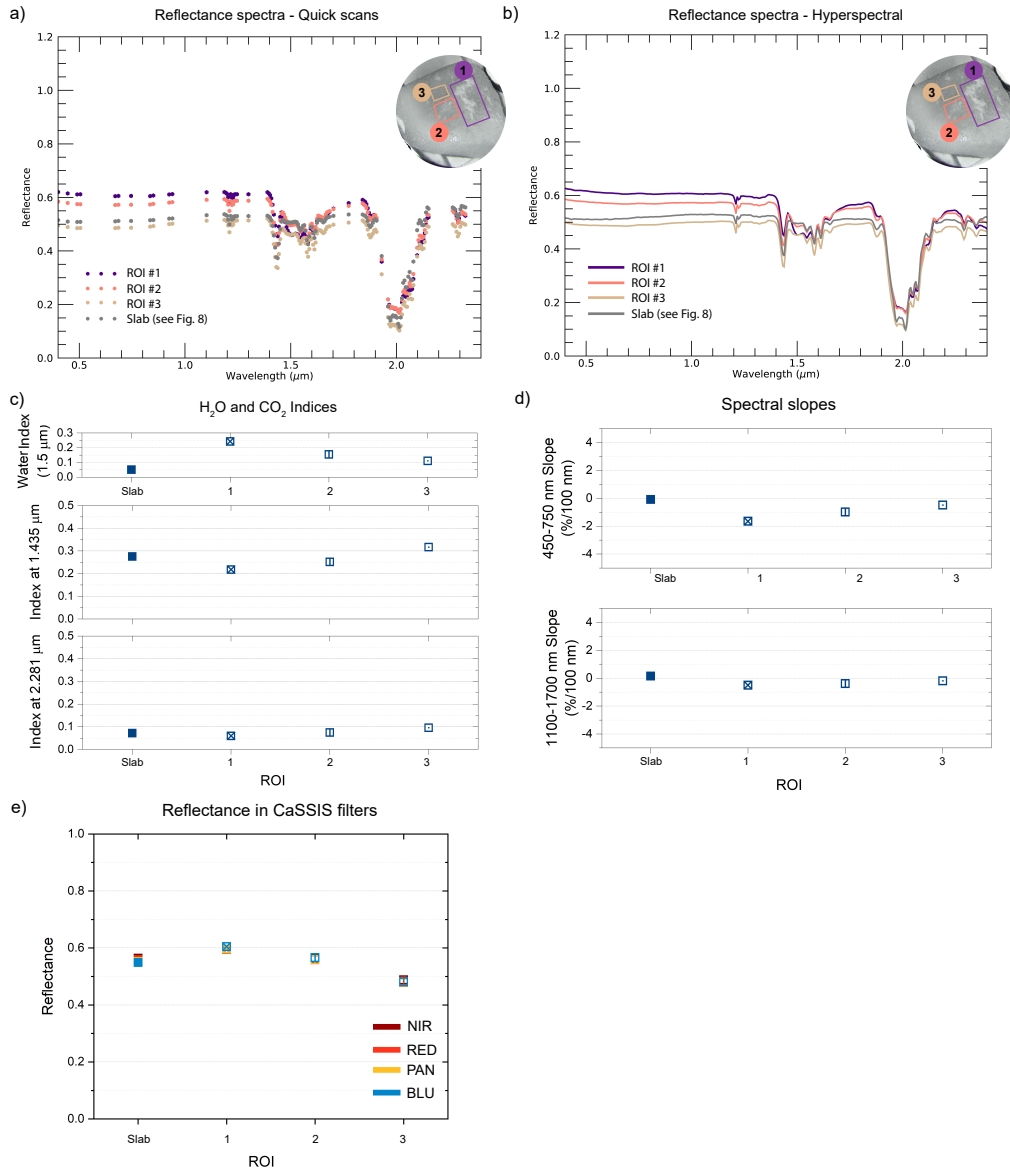


Figure 9: Water frost over CO<sub>2</sub> slab with different amount/thickness of frost within three ROIs identified on the RGB colour composite. a) Multispectral reflectance spectra of the ROIs. b) Hyperspectral reflectance spectra of the ROIs. c) Strength of various absorption features: the one from H<sub>2</sub>O at 1.5 μm and the ones at 1.435 and 2.281 μm from CO<sub>2</sub> ice. d) VIS and NIR spectral slopes of the ROIs. e) Simulated reflectance measured in the CaSSIS filters. Based on the observed strengths of the 1.5 μm band compared to earlier experimental work, we estimate the frost thicknesses in the three ROIs (# 1, 2 and 3) to be 400, 150 and 75 μm, respectively.

## CO<sub>2</sub> and H<sub>2</sub>O ice. Intimate mixtures I

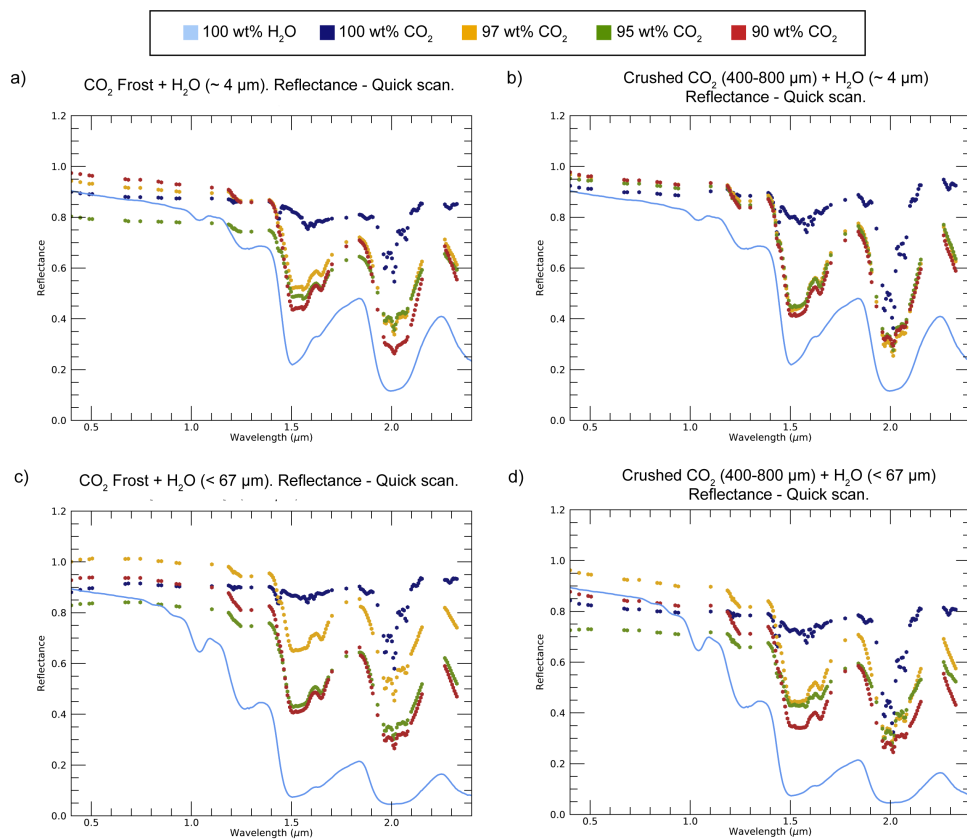


Figure 10: Multispectral (quick scans) spectra of intimate mixtures of CO<sub>2</sub> and H<sub>2</sub>O ices. The legend shows the CO<sub>2</sub> content of each sample. a) CO<sub>2</sub> frost with fine grained H<sub>2</sub>O ice (~ 4 μm). b) Crushed CO<sub>2</sub> with fine grained H<sub>2</sub>O ice (~ 4 μm). c) CO<sub>2</sub> frost with coarser grained H<sub>2</sub>O ice (< 67 μm). d) Crushed CO<sub>2</sub> with coarser grained H<sub>2</sub>O ice (< 67 μm).

## CO<sub>2</sub> and H<sub>2</sub>O ice. Intimate mixtures II

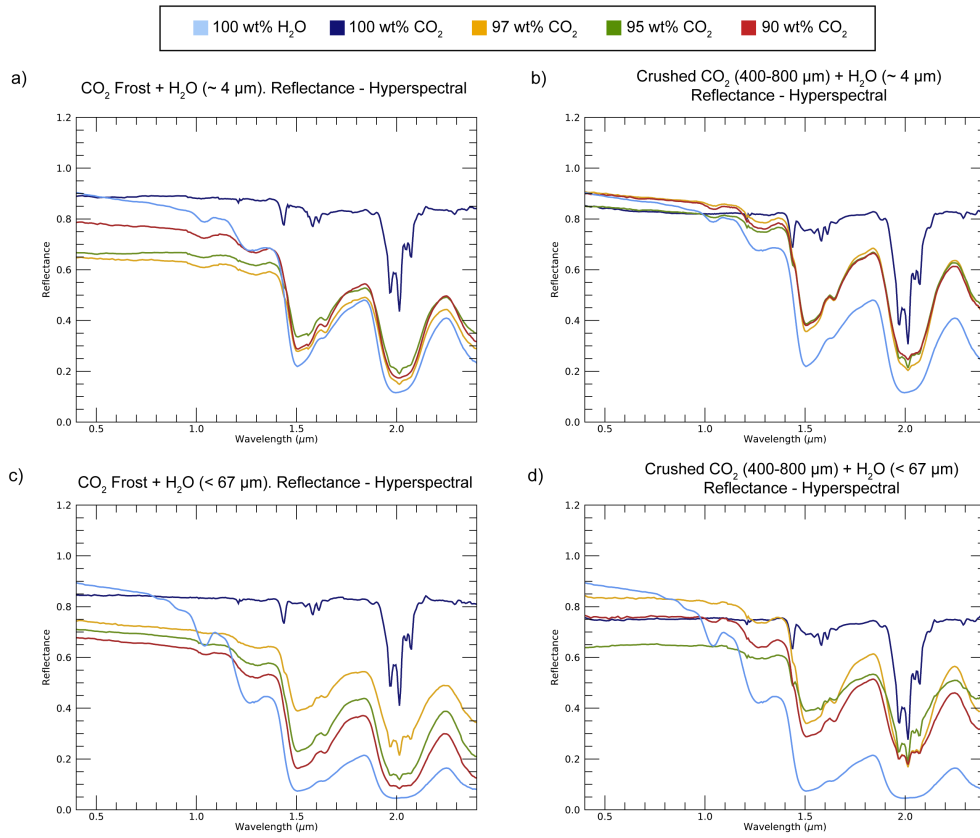


Figure 11: Hyperspectral spectra of intimate mixtures of CO<sub>2</sub> and H<sub>2</sub>O ices. The legend shows the CO<sub>2</sub> content of each sample. a) CO<sub>2</sub> frost (10-100 μm) with fine grained H<sub>2</sub>O ice (~ 4 μm). b) Crushed CO<sub>2</sub> with fine grained H<sub>2</sub>O ice (~ 4 μm). c) CO<sub>2</sub> frost with coarser grained H<sub>2</sub>O ice (~ 67 μm). d) Crushed CO<sub>2</sub> with coarser grained H<sub>2</sub>O ice (~ 67 μm).

### CO<sub>2</sub> and H<sub>2</sub>O ice. Intimate mixtures III

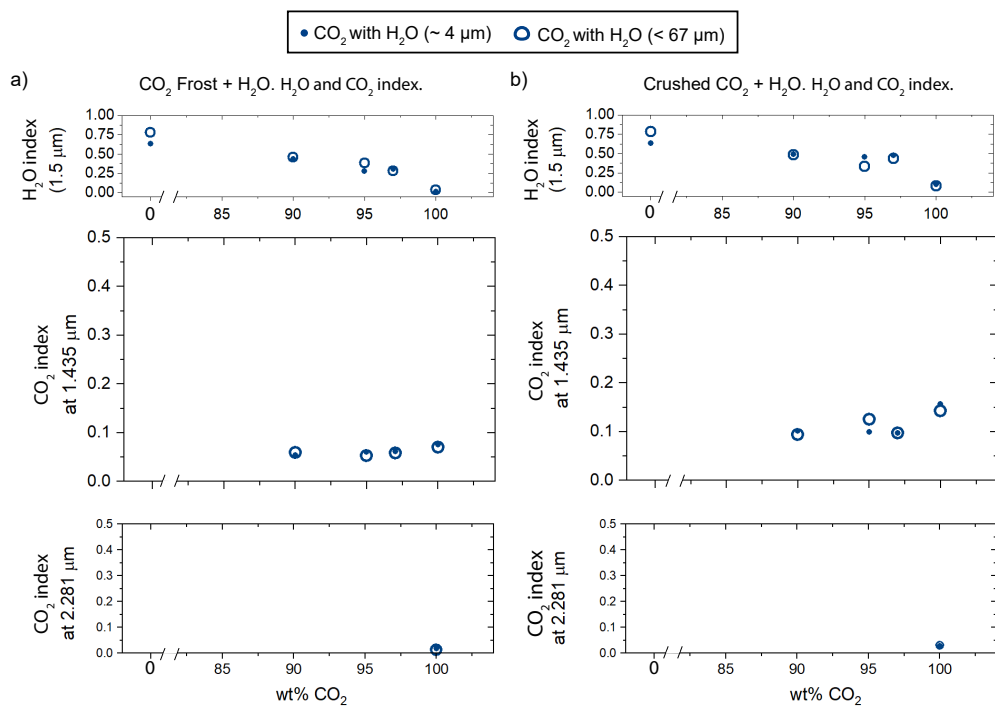


Figure 12: Analysis of different spectral criteria for intimate mixtures of CO<sub>2</sub> and H<sub>2</sub>O ices in the form of H<sub>2</sub>O ice particles of either ~ 4 μm or ~ 67 μm (full vs. open symbols), a) Using CO<sub>2</sub> frost (10-100 μm). b) Using crushed CO<sub>2</sub> (400-800 μm)

## CO<sub>2</sub> and H<sub>2</sub>O ice. Intimate mixtures IV

● CO<sub>2</sub> with H<sub>2</sub>O (~ 4 μm)    ○ CO<sub>2</sub> with H<sub>2</sub>O (< 67 μm)

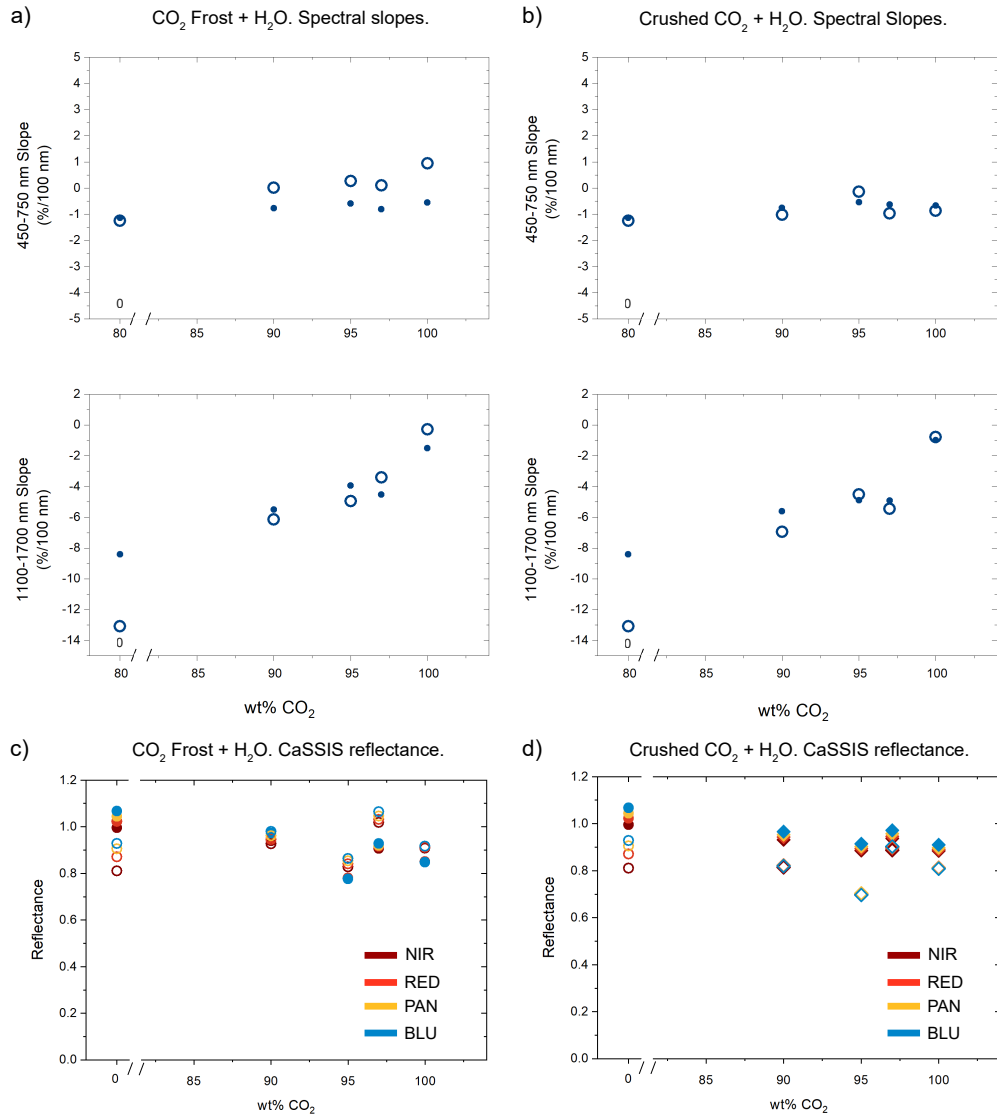


Figure 13: Analysis of spectral criteria for intimate mixtures of H<sub>2</sub>O ice and CO<sub>2</sub> ice in the form of left) frost (10-100 μm) or right) crushed particles between 400 and 800 μm. a) and b) Visible (top) and near-IR (bottom) spectral slopes. c) and d) Simulated reflectance with the CaSSIS filters.

Crushed CO<sub>2</sub> (400-800 μm) and JSCM-1 intimate mixtures.

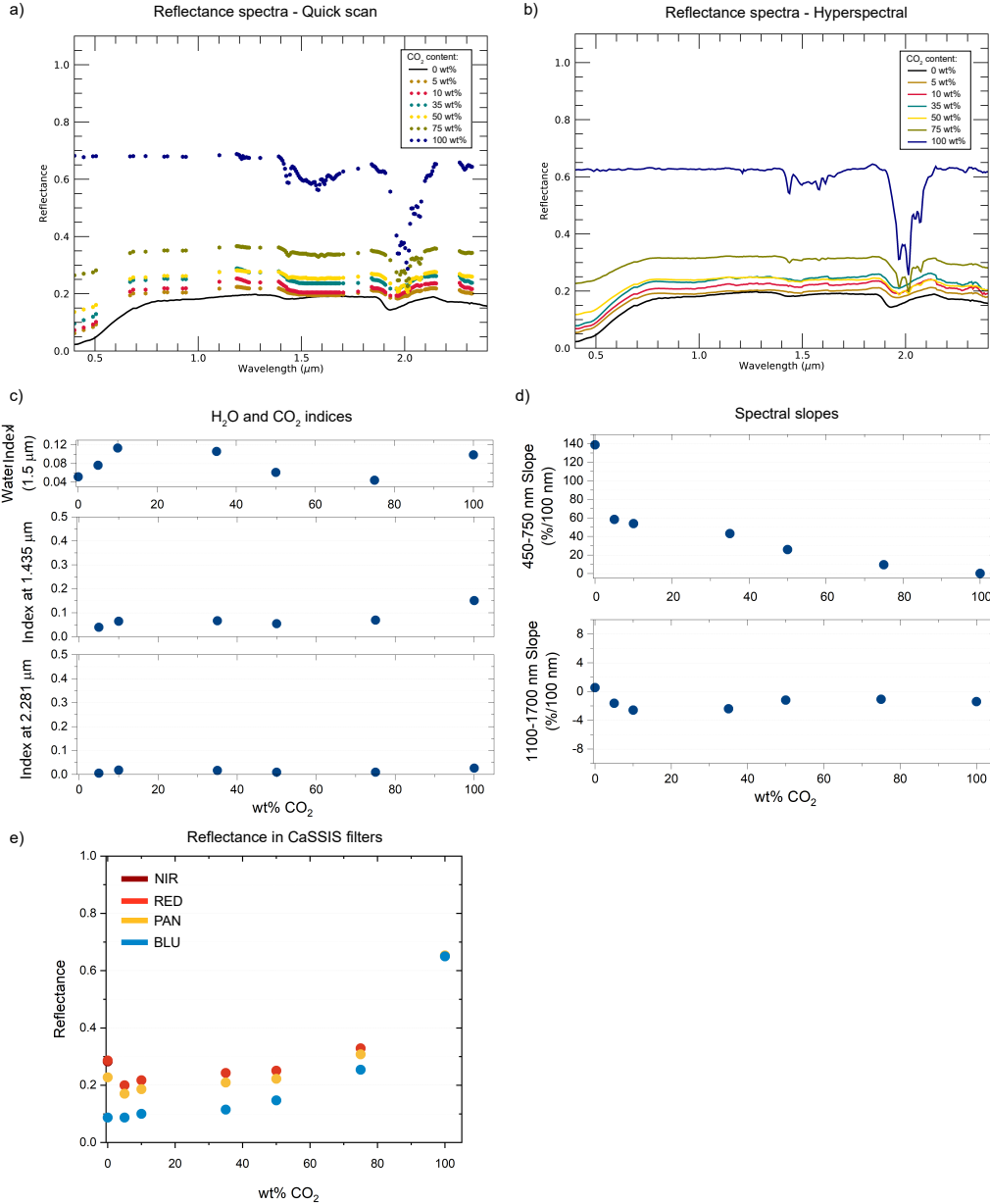


Figure 14: Reflectance analysis of crushed CO<sub>2</sub> ice and JSC Mars-1 intimate mixtures. a) Multispectral (quick scans) reflectance spectra. b) Hyperspectral reflectance spectra c) Strength of various absorption features: the one from H<sub>2</sub>O at 1.5 μm (indicative of the cold-trapped water) and the ones at 1.435 and 2.281 μm from CO<sub>2</sub> ice. d) VIS and NIR spectral slopes of the samples. e) Simulated reflectance measured in the CaSSIS filters.

Sublimation series of CO<sub>2</sub> and H<sub>2</sub>O ice with JSCM-1.

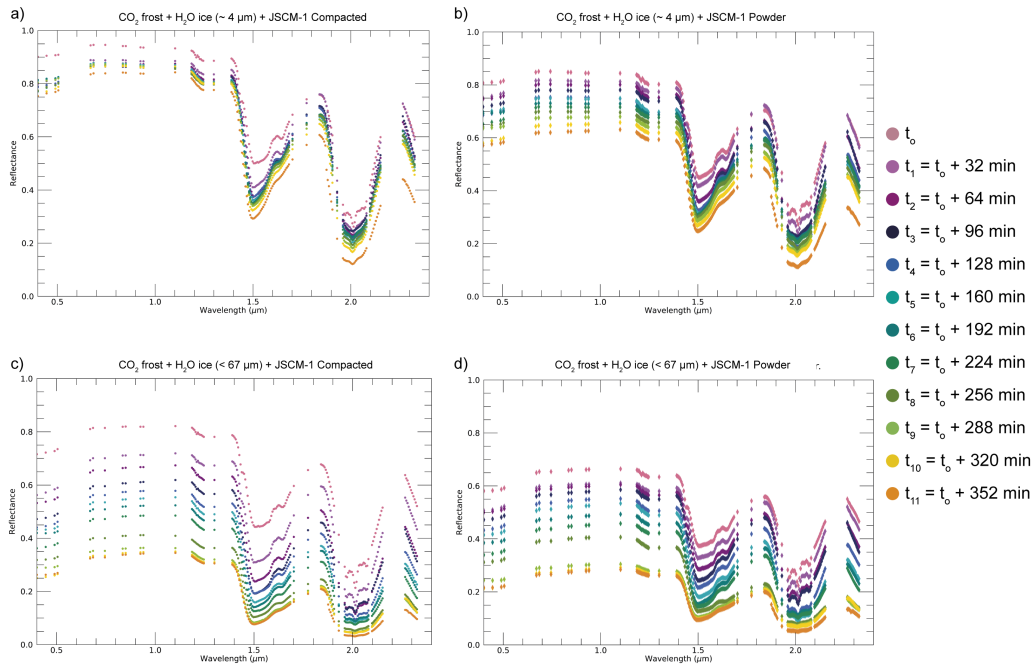


Figure 15: Reflectance spectra of ternary intimate mixtures (CO<sub>2</sub> and H<sub>2</sub>O ice with JSC Mars-1). a) Compacted mixture of CO<sub>2</sub> frost (10-100 μm), fine grained H<sub>2</sub>O ice (~ 4 μm) and JSC Mars-1. b) Powdered mixture of CO<sub>2</sub> frost, fine grained H<sub>2</sub>O ice and JSC Mars-1. c) Compacted mixture of CO<sub>2</sub> frost, coarser grained H<sub>2</sub>O ice (~ 67 μm) and JSC Mars-1. d) Powdered mixture of CO<sub>2</sub> frost, coarser grained H<sub>2</sub>O ice and JSC Mars-1.

Sublimation series of CO<sub>2</sub> and H<sub>2</sub>O ices with JSC Mars-1

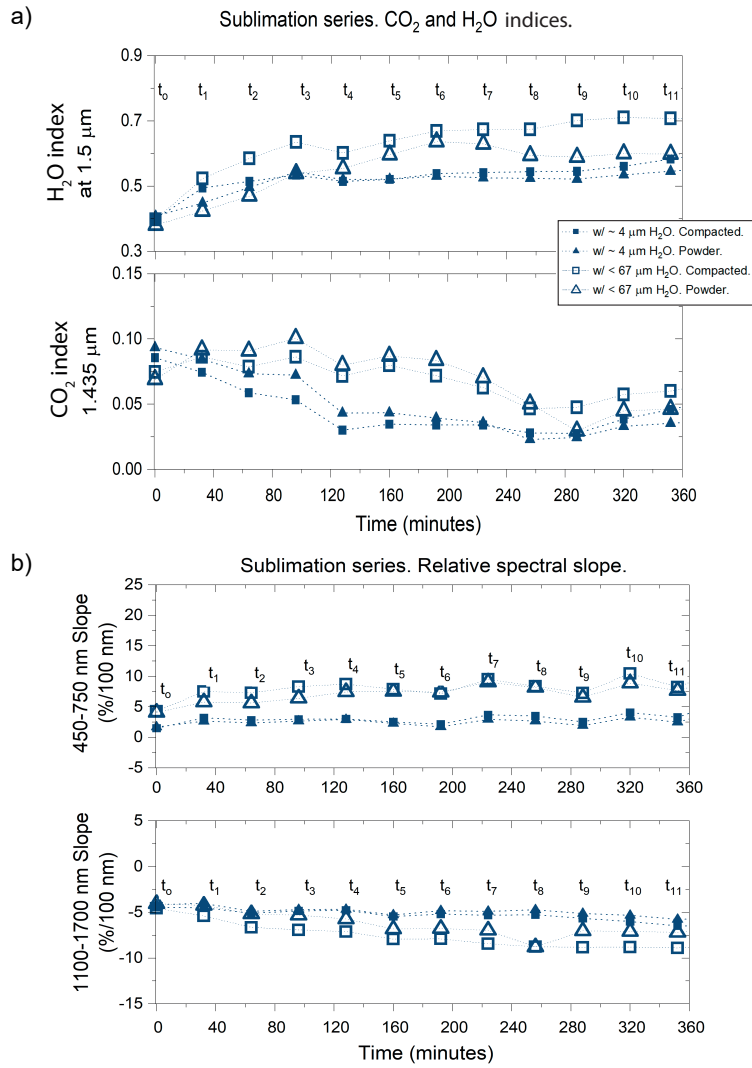


Figure 16: Analysis of spectral criteria of ternary mixtures of CO<sub>2</sub>/H<sub>2</sub>O ice with JSC Mars-1. a) Analysis of the water (1.5 μm) and carbon dioxide (1.435 and 2.281 μm) indices. b) VIS (top) and NIR (bottom) spectral slopes.

- i) ■ CO<sub>2</sub> Slab  
◆ CO<sub>2</sub> Granulated  
⊠ CO<sub>2</sub> Slab with H<sub>2</sub>O frost  
◊ Intimate mixture: CO<sub>2</sub> + H<sub>2</sub>O  
◆ Intimate mixture: CO<sub>2</sub> + JSCM-1  
● Ternary mixture: CO<sub>2</sub> + H<sub>2</sub>O + JSCM-1
- ii) ● H<sub>2</sub>O Granulated  
× H<sub>2</sub>O Frost over JSCM-1  
● Intimate mixture: JSCM-1 + H<sub>2</sub>O  
□ Frozen soil JSCM-1  
▲ JSCM-1

Figure 17: Legends applicable to Figs. 18 and 19. i) Legend applicable to the CO<sub>2</sub> experiments. ii) Legend applicable to the H<sub>2</sub>O experiments, imported from [56]

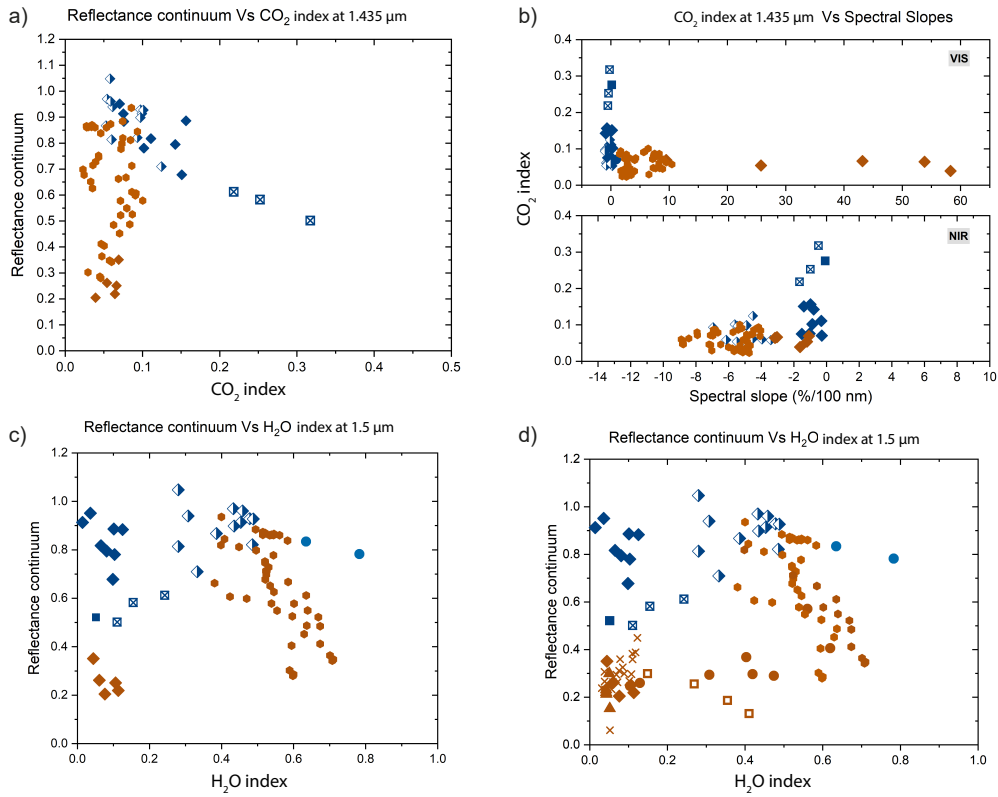


Figure 18: Comparison of spectral criteria between experiments. Addition of H<sub>2</sub>O/dust experiments from [56]. The legend for these plots is provided in Figure 17. Tip: the colours inform about the composition of the samples, and the symbols about their mixing mode/texture a) Reflectance of the continuum v. CO<sub>2</sub> index (1.435 μm). b) CO<sub>2</sub> index (1.435 μm) VS the VIS (top) and NIR (bottom) spectral slopes. c) Reflectance of the continuum VS the H<sub>2</sub>O index (1.5 μm). d) Same as c) with water ice/dust experiments.

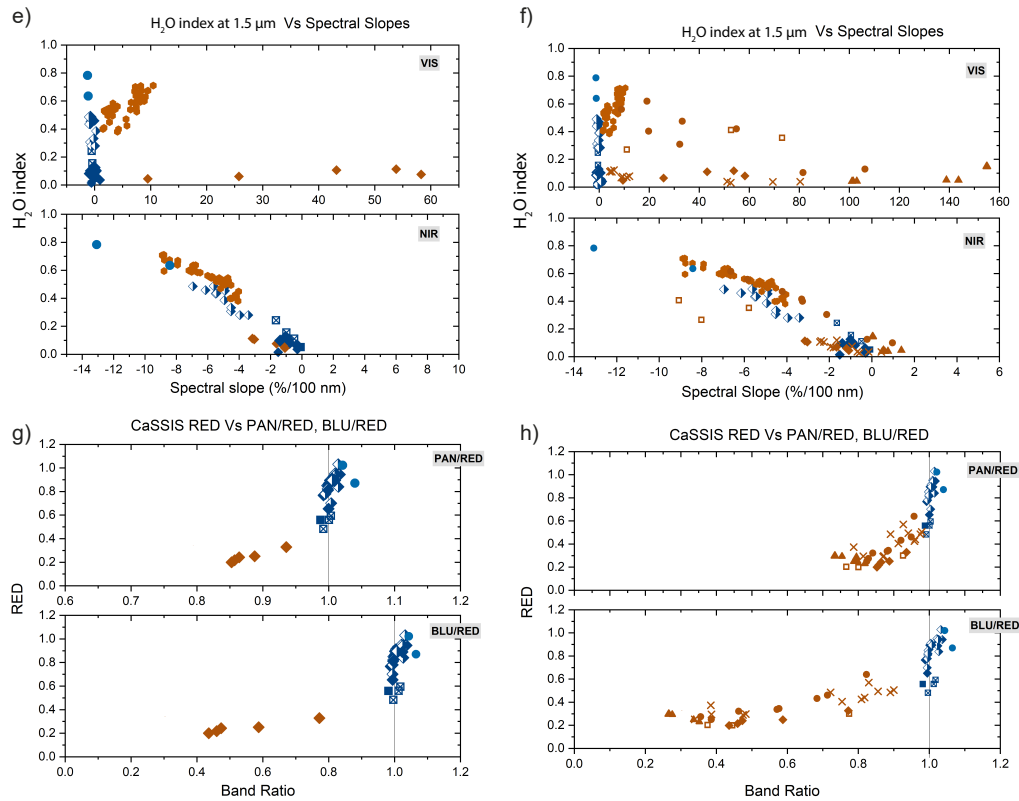


Figure 19: Continuation of Figure 18. Comparison of spectral criteria between experiments. Addition of H<sub>2</sub>O/dust experiments from [56]. The legend for these plots is shown in Figure 17 e) Water index at 1.5 μm versus the VIS (top) and NIR (bottom) spectral slopes. f) Same as e) with water ice/dust experiments. g) Reflectance simulated in the RED filter of CaSSIS versus the PAN/RED (top) and BLU/RED (bottom) ratios. h) Same as g) with the water ice /dust experiments.

## 4. Discussion

### 4.1. Spectro-photometry of pure CO<sub>2</sub>

We have measured the spectra of various size fractions of CO<sub>2</sub> ice in the spectral range 0.4-2.4  $\mu\text{m}$ . According to Singh and Flanner [19], in a semi-infinite layer, the size of the CO<sub>2</sub> ice grains affects less the reflectance than the size of H<sub>2</sub>O ice. In our experiments however, the samples were only 2-cm thick. While the particles of the CO<sub>2</sub> frost (10-100  $\mu\text{m}$ , see Fig. 2) are small enough that this particular sample is optically thick (see the discussion of this topic by Hapke [18]), the dark neutral substrate of the sample holder (constant reflectance of 0.05) certainly affects the continuum level of the slab and crushed slab samples. Indeed, because of the low absorptivity of CO<sub>2</sub> in the continuum, photons were able to reach the bottom of the sample holder. The fact that the samples are not optically thick probably explains the dependence of continuum reflectance on particle size. But with the exception of the slab sample (reflectance reduced to 0.5), the effects of the substrate are relatively minor, with a maximum decrease of reflectance of 0.2 only between the coarsest fraction (400-800  $\mu\text{m}$ ) and the optically thick snow. This is less than what would be expected from models which predict a very high transparency of samples made of such large CO<sub>2</sub> particles [19]. The fine-scale texture at the surface of the grains as well as the presence of interfaces, pores or defects in the interiors of the grains probably increases the scattering and decreases the penetration compared to idealised smooth and compact particles. The situation is different at wavelengths where the absorption is not negligible and the variations of the absorption bands intensity between the different particle size fractions are essentially the results

of the change of particle size. However, spectral criteria such as band depth which consist essentially in a contrast of reflectance between the band and the continuum will still be affected. Therefore, care must be taken when comparing directly these spectra of pure CO<sub>2</sub> ice with Martian spectra but as the reflectance of the substrate and the thickness of the samples are known, these spectra remain nevertheless useful to compare to the outputs of models and simulation.

Our spectra of crushed CO<sub>2</sub> ice show a strength of the 2  $\mu\text{m}$  band similar to the one of the "fractured layer" shown by [48]. We see much more structure in this band, however, probably because of the higher spectral resolution of our measurements. Similarly we see strong but narrow absorption at 1.44 and 1.6  $\mu\text{m}$ , which are not visible in the spectrum of [48]. Our spectrum of CO<sub>2</sub> frost (10-100  $\mu\text{m}$ ) appears very similar to the one labeled as "medium-grained" in [48] despite the same differences as observed with crushed CO<sub>2</sub>, again probably because of the different spectral resolution. While there is no estimate for how large this "medium-grained" frost is, it is larger than the "fine-grained" CO<sub>2</sub> frost which displays surface texture at the 10-20  $\mu\text{m}$  scale. This is consistent with the microscope observations of our CO<sub>2</sub> frost which show large particles of a few tens of  $\mu\text{m}$  in diameter.

Note that on planetary surfaces as in the laboratory, different grain sizes can lead to different capacities of atmospheric water frost trapping, which also indirectly affect the reflectance of the samples.

Regardless of the grain size, CO<sub>2</sub> is overall poorly absorptive in the studied spectral range, with some deep but narrow absorption bands longward of 1.1  $\mu\text{m}$ . In our laboratory spectra, CO<sub>2</sub> presents flat visible spectra; Singh

and Flanner [19] modelled, however, a red slope at wavelengths shorter than 0.5  $\mu\text{m}$ , which we have not been able to reproduce, possibly due to the contamination of the surface of the samples by  $\text{H}_2\text{O}$  frost.

Further comparison between modeling results [19] and our experimental spectra show other differences. In particular, the strength of the  $\text{CO}_2$  absorption bands in our spectra are consistent with modeled spectra of much smaller particle size. For instance, our spectrum for the (400-800)  $\mu\text{m}$  size fraction displays a band depth of about 0.5, similar to the modeled spectrum with a particle size of 100  $\mu\text{m}$  in the work of Singh and Flanner [19]. Also surprisingly, the spectrum of our compact slab shows band strengths much smaller than the modeled spectrum for a particle diameter of 1.5mm and seems more consistent with a modeled grain size of 500  $\mu\text{m}$  only. These discrepancies between experimental and modeled results probably originate from the non-ideal particles produced for the experiments that display irregularities in shape, fine-scales surface texture, internal defects, pores and joints between grains. All these features of complex real particles combine to scatter the light at scales much smaller than the actual diameter of spherical particles assumed in models.

#### *4.2. $\text{CO}_2$ as a component of a mixture*

As part of a mixture, and because of the flat spectrum of  $\text{CO}_2$  ice,  $\text{CO}_2$  acts as a reddening material when mixed with a bluer one (e.g., water), and as a bluing one when mixed with a redder one (e.g., JSC Mars-1). In this regard,  $\text{CO}_2$  ice has similar effects on the reflectance spectra as the early stages of water frost deposition. Small amounts of water frost condensed on some samples increase the reflectance and flatten the spectral slopes of the

materials underneath, without producing any significant increase in the H<sub>2</sub>O indexes [56]. Unfortunately, these similarities complicate the differentiation of CO<sub>2</sub> and H<sub>2</sub>O frosts from analysis of visible colours only.

In the first paper of this series, we showed how small amounts of JSC Mars-1 were enough to mask water ice when both materials were intimately mixed. Here, we observe how small amounts of water ice intimately mixed with carbon dioxide ice can mask the CO<sub>2</sub>. This is not a new result as it was already shown experimentally by Kieffer [49] (from 0.8  $\mu\text{m}$ ) and predicted theoretically [71].

We explained in Yoldi et al. [56] that the reflectance of water ice and dust intimate mixtures does not increase linearly with the amount of water ice. Instead, the spectra of intimate mixtures are controlled by the most absorptive component. JSC Mars-1 is the absorptive material when mixed with H<sub>2</sub>O ice, but when we mix H<sub>2</sub>O and CO<sub>2</sub> ices, water ice is the most absorptive material. Consequently, the reflectance spectra of intimate mixtures of water and carbon dioxide ices are dominated by water ice. This situation reverses at wavelengths where water becomes less absorptive than CO<sub>2</sub>. Parameters such as grain size or association mode between the materials can balance this behaviour of the reflectance spectra [56, 71, 19]. It is still important to remember that, when looking at planetary surfaces in the 0.4-2.4  $\mu\text{m}$  spectral range, a surface showing a water-like spectrum is not necessarily free of CO<sub>2</sub>, in the same way as a surface showing a dust spectrum does not exclude the presence of ice [21].

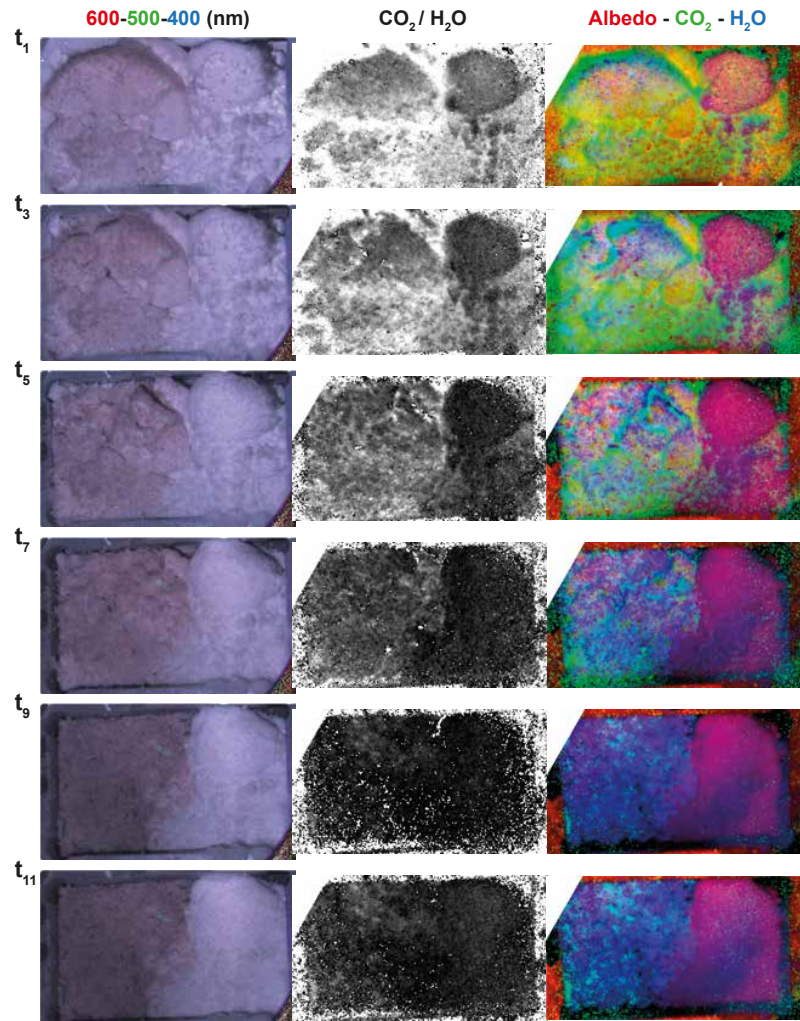


Figure 20: Sublimation series of the ternary mixtures of  $\text{CO}_2$  frost (10-100  $\mu\text{m}$ ), water ice (fine and coarser grained, respectively) and JSC Mars-1. In the left column, we show RGB composites with the signal at 600 nm in the red channel, at 500 nm in the green channel and 400 nm in the blue channel. The column in the middle is a monochromatic image containing the  $\text{CO}_2/\text{H}_2\text{O}$  ratio. The images in this column are stretched from 0.02 to 0.3. The right column shows RGB composites with the continuum reflectance in the red channel, the  $\text{CO}_2$  index in the green channel and the  $\text{H}_2\text{O}$  index in the blue channel. Stretching:  $R(0.318-0.520)$ ,  $G(0.214-0.306)$ ,  $B(0.339-0.575)$ . The rows correspond to the samples at odd times between  $t_1$  and  $t_{11}$ .

### 4.3. Ternary mixtures of $CO_2$ , $H_2O$ and JSC Mars-1

Fig 20 shows half of the steps of the sublimation process of ternary mixtures. The complete sequence can be found, in video format, in the supplementary material. We have produced RGB colour composites with three wavelengths (600, 500 and 400 nm) and three spectral parameters (reflectance in the continuum,  $CO_2$  signature and  $H_2O$  signature), as well as monochromatic images representing the  $CO_2$ -to- $H_2O$  ratio.

The images on the left column of Fig 20 provide a good approximation to the natural colours of the samples and reveal a different evolution of the mixture with fine grained ( $\sim 4.5 \mu\text{m}$ , right) and coarser grained ( $\sim 67 \mu\text{m}$ , left)  $H_2O$  ice. The mixture with fine  $H_2O$  ice particles looks brighter than the one with coarser  $H_2O$  ice particles since the scattering by the small particles dominates the reflectance throughout the entire sequence. Besides the brightness, we observed a distinct evolution of the texture and morphology of the samples. In the mixtures with coarser  $H_2O$  ice particles, the compacted sample (top of the image, see Fig 2.1.3) broke apart as the volatile components sublimated. At the same time, JSC Mars-1 deposited on top of the mixtures, conferring to the sample its characteristic reddish colour. Thus, the sample with coarser  $H_2O$  ice appears in  $t_{11}$  as an almost flat deposit of JSC Mars-1 mixed with the remaining water ice. The sample with finer  $H_2O$  ice, however, seemed to have undergone a process of expansion (this is best appreciated on the video): while in  $t_1$  we can still identify the flat surface of the compacted sample, from  $t_5$  the sample resembles a porous snowball because of the ice filaments it has grown on the surface. The powdered sample (below the compacted one) went through the same process, which

progressively softened its surface.

The images on the column in the middle show the evolution of the  $\text{CO}_2/\text{H}_2\text{O}$  ratio as both sublimated. The pictures have been stretched so that black corresponds to  $\text{CO}_2/\text{H}_2\text{O} = 0.02$  and white to  $\text{CO}_2/\text{H}_2\text{O} = 0.3$ .  $t_1$  already presents the samples bearing fine ice slightly darker than the ones with coarse ice. This contrast increases with time so that at  $t_5$  the signatures of water already dominate the spectrum of the samples where  $\text{H}_2\text{O}$  ice is fine grained ( $4.5 \mu\text{m}$ ). The images at  $t_9$  and  $t_{11}$ , although noisy, show a little brightening of the samples, related to the increase in the  $\text{CO}_2$  signal we measured in Figure 16a. Finally, the RGB composites of spectral criteria give an overview of the evolution of the albedo and the  $\text{CO}_2$  and  $\text{H}_2\text{O}$  signatures, represented by the red, green and blue colours, respectively. The colours reveal that, from  $t_5$ , a layer of water covers the fine-grained mixtures, while green tones are still visible in the coarse-grained ones. In the pictures from  $t_7$  and  $t_9$ , we observe that  $\text{CO}_2$  remains preferentially in the creases of the material, and in  $t_{11}$ , the strengthening of the signal of  $\text{CO}_2$  appears as sparse green dots.

From the information that these images provide, we have reconstructed the process of sublimation of the ternary mixtures (Fig 21). In the beginning ( $t_1 \sim 160 \text{ K}$ ), the main component subject to sublimation is  $\text{CO}_2$ . As it sublimates in the mixture with coarser  $\text{H}_2\text{O}$  ice particles, the surface concentrations of water ice and JSC Mars-1 increase. Around  $t_5$  ( $\sim 195 \text{ K}$ , i.e., the sublimation temperature of  $\text{CO}_2$  ice at 1 atm), all the  $\text{CO}_2$  has sublimated from the surface and the water ice and JSC Mars-1 form a mantle that protects the  $\text{CO}_2$  ice underneath from rapid sublimation. In the mix-

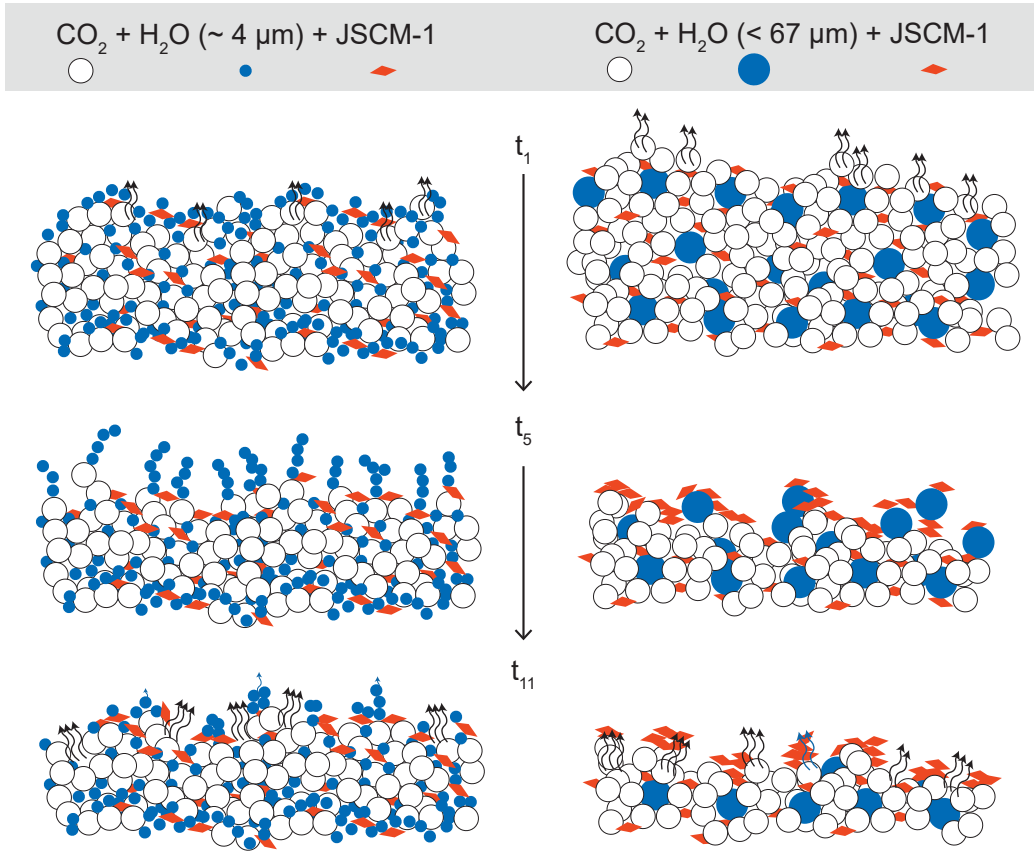


Figure 21: Schematic view of the sublimation processes for ternary mixtures of  $\text{CO}_2$  frost ( $10\text{-}100\ \mu\text{m}$ ),  $\text{H}_2\text{O}$  ice (two different particle sizes) and a finer fraction ( $< 100\ \mu\text{m}$ ) of the JSC Mars-1 regolith simulant. To the left, mixtures with fine  $\text{H}_2\text{O}$  ice particles ( $\sim 4.5\ \mu\text{m}$ ) and to the right with coarser ( $\sim 67\ \mu\text{m}$ ) particles. The three rows represent different times in the sublimation process, increasing from top to bottom and corresponding approximately to  $t_1$ ,  $t_5$  and  $t_{11}$  on Fig 20. As  $\text{CO}_2$  ice (blue particles) sublimates, the JSC Mars-1 dust analogue (red) accumulates at the surface in both cases. The process of sublimation seems to differ depending on the size of the water particles. In the case of coarse ( $\sim 67\ \mu\text{m}$ )  $\text{H}_2\text{O}$  particles, they simply accumulate at the surface and eventually sublimate. The fine ( $\sim 4.5\ \mu\text{m}$ )  $\text{H}_2\text{O}$  ice particles display a different behaviour as they clump together, forming long and thin filaments of water ice which progressively cover most of the surface but are occasionally ejected by the flux of  $\text{CO}_2$  gas produced by the sublimation of the ice.

tures with fine  $\text{H}_2\text{O}$  ice, however, when the grains of  $\text{CO}_2$  sublimate, they carry along the fine grains of water ice. As the  $\text{CO}_2$  gas expands, it cannot

hold the water ice grains any longer, which fall again onto the sample. The grains of fine H<sub>2</sub>O ice rearrange then in energetically suitable structures, in this case, filaments (t<sub>5</sub>). This step explains the change of texture seen in these mixtures, which seemed to grow fluffy. These filaments are effective light-scatters; their signal dominates the reflectance and masks the CO<sub>2</sub> ice underneath.

As the temperature in our experiment kept increasing, the sublimation accelerated. At some point (in our case t<sub>9</sub> or t<sub>11</sub>), the pressure of the sublimating CO<sub>2</sub> gas was strong enough to clear its way out of the sample, piercing the sublimation lag and/or breaking the water ice structures. Some of the inner CO<sub>2</sub> grains then became visible at the places where this process had just occurred.

This sequence of differential sublimation explains why the CO<sub>2</sub> index does not drop linearly with sublimation (see Fig 16). Instead, the signal first drops, levels out and then increases for mixtures with fine grained H<sub>2</sub>O ice and oscillates in the beginning to then drop and again rise for mixtures with coarser H<sub>2</sub>O ice. It also explains why the H<sub>2</sub>O signal does not increase linearly, but initially increases to eventually level out (fine H<sub>2</sub>O) or slow down (coarser H<sub>2</sub>O). The growth of the CO<sub>2</sub> signal once it seemed to be gone could also be explained by the release of previously adsorbed CO<sub>2</sub> on JSC Mars-1 microparticles or possibly by the decomposition of CO<sub>2</sub> clathrate hydrates (Vincent Chevrier, personal communication). Presumably, how this sublimation sequence develops depends on factors such as the CO<sub>2</sub>-to-H<sub>2</sub>O ratio, the grain size of the refractory material or the association mode of the materials (as seen in Poch et al. [72]).

Finally, these experiments provide experimental support for the hypothesis formulated in Appéré et al. [42] and Pommerol et al. [45] regarding the disappearance and subsequent return of the spectral signal of CO<sub>2</sub>. A thin mantle of fine water frost masks the signature of CO<sub>2</sub>, which reappears as the water frost layer disrupts with the increase of temperature.

#### *4.4. Use of spectral parameters to identify mixtures*

To identify CO<sub>2</sub> ice, the first thing to look for is its absorption feature at 1.435  $\mu\text{m}$ . As we have repeatedly noted, the detection of a CO<sub>2</sub> signature evinces the presence of that component, but the lack of a signature does not guarantee the absence of CO<sub>2</sub> since it could be mixed intimately with other components (e.g., water ice) and masked. We can also get a hint about the presence of CO<sub>2</sub> ice by looking at the continuum reflectance against the water index at 1.5  $\mu\text{m}$  (Fig 18d); CO<sub>2</sub>-bearing experiments stand out with high reflectance at weak water indices.

*CO<sub>2</sub> Vs. CO<sub>2</sub> + dust.* To identify dust in the mixtures, looking at the CaSSIS colours provide a direct answer. Indeed, every sample containing JSC Mars-1 falls under BLU/RED ratios of 0.9, while pure ice samples fall around BLU/RED ratios of 1.0. Alternatively, comparing the visible spectral slope to either the water or the carbon dioxide indexes is a good strategy to identify most of the JSC Mars-1 - bearing samples.

*CO<sub>2</sub> Vs. CO<sub>2</sub> + H<sub>2</sub>O.* In order to identify water ice, we look at the H<sub>2</sub>O index; for example, by comparing the visible spectral slope against the water index. Comparing first the water index to the visible spectral slope and then to the NIR spectral slope allows us first to identify pure ice samples, and then

to identify whether the samples are made of pure water ice, intimate mixtures of carbon dioxide and water ices or pure carbon dioxide. Looking at the CO<sub>2</sub> index versus the NIR spectral slope also allows us to differentiate between intimate mixtures of water and carbon dioxide ices, pure CO<sub>2</sub> samples and slabs.

*Atmospheric frost.* In our previous publication, we pointed out the comparison of the H<sub>2</sub>O index and the visible slope as being useful to identify water frost [56]. When we incorporate the CO<sub>2</sub> experiments, this identification becomes more difficult, since CO<sub>2</sub> and small condensates of water frost share the same reflectance characteristics: they are bright, they tend to flatten the spectral slope of the substrate they are mixed with, and they do not alter the absorption bands of water. Therefore, it is hard to tell whether the intimate mixtures with JSC Mars-1 have trapped water frost by looking at Fig 19f (VIS). We have to look as well at the near-infrared, where water and carbon dioxide behave differently, water being bluer than carbon dioxide. In Fig 19f (NIR) we observe that two of the symbols for CO<sub>2</sub> and JSC Mars-1 intimate mixtures in the graph at the bottom follow the trend drawn by the JSCM-1/water frost experiments instead of remaining with the pure CO<sub>2</sub> or pure JSC Mars-1 samples. The corresponding experiments have indeed trapped water frost.

#### 4.5. *Limitations of the measurements.*

As mentioned in Section 2, it is challenging to achieve homogeneous intimate mixtures in which the end members are present in extreme ratios (i.e., 10 wt% - 90 wt% instead of 50 wt%- 50 wt%). The task becomes even more

challenging when both components have the same colour since we cannot assess visually how well they mix. The measured reflectance showed that we succeeded in obtaining different CO<sub>2</sub>-to-H<sub>2</sub>O ratios. However, due to the formation of agglomerates, the samples were not as homogeneous as desired (see for example Fig 4a). Kieffer [49] already noted the difficulty of linking the reflectance spectra to the composition of his samples, due to textural effects. In the same way, we are not able to identify the mixtures displaying more water ice from their reflectance in the visible. In the near-infrared, however, the presence of the absorption bands of water allows us to notice the increasing amount of water ice within the samples.

Because of the fast sintering of CO<sub>2</sub> ice grains, fine granular surfaces are hard to achieve [73]. Further laboratory work is needed to achieve CO<sub>2</sub> samples free from agglomerates, to first study their reflectance with smooth surfaces, and then understand the nature of agglomerates as well as their effect on the reflectance. We need to understand, for instance, whether we are creating these agglomerates by manipulating the samples, whether they only form at atmospheric pressures or whether small granular sliding at the surface of ice is enough to create them.

## 5. Conclusions

We have reported on the reflectance measurements carried out at LOSSy on analogues for the surface of Mars containing H<sub>2</sub>O and CO<sub>2</sub> ice (at atmospheric pressure). We have measured the reflectance of pure CO<sub>2</sub> frost, ice grains and slabs, and we have mixed CO<sub>2</sub> with water ice (intimate mixture and as frost contamination) and/or JSC Mars-1. We have monitored the reflectance of a ternary mixture of CO<sub>2</sub>, H<sub>2</sub>O and JSC Mars-1 as the volatile components sublimated. We summarise below the general trends we've observed:

- The size of particles of CO<sub>2</sub> plays a key role in the reflectance in various ways. i) Large particles transport photons deep in the medium, while small particles scatter light more efficiently, masking the material underneath the ice ii) Small particle sizes trap more of atmospheric water.
- The reflectance in the visible of the mixtures with granulated CO<sub>2</sub> is dominated by effects of the texture rather than the composition itself. In the near-infrared, however, the composition drives the reflectance.
- As a part of a mixture, CO<sub>2</sub> is easily masked by more absorbent components due to its weak absorptivity. The materials tested here (water ice and JSC Mars-1) being much more absorptive than CO<sub>2</sub>, masked the characteristic absorption features of CO<sub>2</sub> out of proportion to their presence.
- The evolution of the reflectance of our ternary mixtures as temperature increased was controlled by the size of the particles of water ice,

even if present only at 3 wt%. The sublimation of CO<sub>2</sub> caused the JSC Mars-1 and coarse-grained water ice to settle down and cover the ice underneath. The sublimation of CO<sub>2</sub> also caused the fine-grained water ice to form highly-scattering H<sub>2</sub>O frost filaments over the CO<sub>2</sub> ice underneath, compatible with the observations of the northern, seasonal, polar cap of Mars by Appéré et al. [42] and Pommerol et al. [45].

- We have compared many spectral parameters in the visible and near-infrared spectral ranges to make our data useful for a wide range of instruments measuring the reflectance of the Martian surface.
- If we want to know about the grain size of the CO<sub>2</sub> ice, it is useful to compare the reflectance in the continuum versus the CO<sub>2</sub> index. To study the colour of the sample is useful to spot dust within the ice samples: CaSSIS colours or comparing the visible spectral slope to the water or carbon dioxide indexes will reveal the presence of dust on a sample. If we compare the water index first to the visible and then to the NIR spectral slope, we can identify if pure ice samples are made only of water ice or carbon dioxide ice or if they are a mix of both.
- It is hard to identify water frost over CO<sub>2</sub> ice by looking at the reflectance spectra of the sample. However, the comparison of the water index versus the visible and NIR spectral slopes is a good indicator of the presence of water frost over surfaces.
- Comparing visible and NIR slopes can be a way of identifying CO<sub>2</sub> ice for instruments that cannot resolve absorption features.

The methods that we have proposed in these two papers (see Yoldi et al. [56]) provide a useful tool to fully exploit reflectance data. Because of the variety of spectral criteria and ranges used, these tools can be used with the data of many instruments that measure or have measured the reflectance of the surface of Mars (i.e., OMEGA, CRISM, HRSC, HiRISE and CaSSIS). They are also useful to calibrate reflectance models. The data here presented are available to the scientific community since these laboratory experiences are critical for the calibration of reflectance models and the understanding of processes occurring on planetary surfaces.

**Data availability** All the reflectance spectra presented here are available on the Bern icY Planetary Analogues Solid Spectroscopy (BYPASS) database, hosted on the Solid Spectroscopy Hosting Architecture of Databases and Expertise (SSHADE) . *Direct DOI link to the data will be provided here upon acceptance.*

**Acknowledgements** This work has been developed in the framework of the National Center for Competence in Research PlanetS funded by the Swiss National Science Foundation (SNSF). The authors want to thank Vincent Chevrier, Aditya Khuller and an anonymous reviewer for their valuable and constructive comments on this article.

## References

- [1] G. Filacchione, A. Raponi, F. Capaccioni, M. Ciarniello, F. Tosi, M. T. Capria, M. C. De Sanctis, A. Migliorini, G. Piccioni, P. Cerroni, M. A. Barucci, S. Fornasier, B. Schmitt, E. Quirico, S. Erard, D. Bockelee-Morvan, C. Leyrat, G. Arnold, V. Mennella, E. Ammannito, G. Bellucci, J. Benkhoff, J. P. Bibring, A. Blanco, M. I. Blecka, R. Carlson, U. Carsenty, L. Colangeli, M. Combes, M. Combi, J. Crovisier, P. Drossart, T. Encrenaz, C. Federico, U. Fink, S. Fonti, M. Fulchignoni, W.-H. Ip, P. Irwin, R. Jaumann, E. Kuehrt, Y. Langevin, G. Magni, T. McCord, L. Moroz, S. Mottola, E. Palomba, U. Schade, K. Stephan, F. Taylor, D. Tiphene, G. P. Tozzi, P. Beck, N. Biver, L. Bonal, J.-P. Combe, D. Despan, E. Flamini, M. Formisano, A. Frigeri, D. Grassi, M. S. Gudipati, D. Kappel, A. Longobardo, F. Mancarella, K. Markus, F. Merlin, R. Orosei, G. Rinaldi, M. Cartacci, A. Cicchetti, Y. Hello, F. Henry, S. Jacquino, J. M. Reess, R. Noschese, R. Politi, G. Peter, Seasonal exposure of carbon dioxide ice on the nucleus of comet 67p/churyumov-gerasimenko, *Science* 354 (2016) 1563–1566.
- [2] D. P. Cruikshank, R. T. L., O. T. C., G. T. R., d. B. C., S. B., B. R. H., B. M. J., Ices on the surface of triton, *Science* 261 (1993) 742–745.
- [3] P. R. Mahaffy, C. R. Webster, S. K. Atreya, H. Franz, M. Wong, P. G. Conrad, D. Harpold, J. J. Jones, L. A. Leshin, H. Manning, T. Owen, R. O. Pepin, S. Squyres, M. Trainer, Abundance and isotopic composition of gases in the martian atmosphere from the curiosity rover, *Science* 341 (2013) 263–266.

- [4] J. B. Pollack, R. M. Haberle, J. Schaeffer, H. Lee, Simulations of the general circulation of the martian atmosphere: 1. polar processes, *Journal of Geophysical Research: Solid Earth* 95 (1990) 1447–1473.
- [5] F. Hourdin, F. Forget, O. Talagrand, The sensitivity of the martian surface pressure and atmospheric mass budget to various parameters: A comparison between numerical simulations and viking observations, *Journal of Geophysical Research: Planets* 100 (1995) 5501–5523.
- [6] P. B. James, H. H. Kieffer, D. A. Paige, The seasonal cycle of carbon dioxide on mars, *Mars* (1992) 934–968.
- [7] B. M. Jakosky, The seasonal cycle of water on mars, *Space science reviews* 41 (1985) 131–200.
- [8] R. Kahn, S. Lee, T. Martin, R. Zurek, The martian dust cycle, in: *Bulletin of the American Astronomical Society*, volume 22, p. 1076.
- [9] S. Piqueux, A. Kleinböhl, P. O. Hayne, N. G. Heavens, D. M. Kass, D. J. McCleese, J. T. Schofield, J. H. Shirley, Discovery of a widespread low-latitude diurnal co<sub>2</sub> frost cycle on mars, *Journal of Geophysical Research: Planets* 121 (2016) 1174–1189.
- [10] G. Neugebauer, G. Münch, H. Kieffer, S. C. J. Chase, E. Miner, Mariner 1969 infrared radiometer results: Temperatures and thermal properties of the martian surface, *Astronomical Journal* 76 (1971) 719.
- [11] R. B. Leighton, B. C. Murray, Behavior of carbon dioxide and other volatiles on mars, *Science* 153 (1966) 136–144.

- [12] S. G. Warren, Optical constants of ice from the ultraviolet to the microwave 23 (1984) 1206–1225.
- [13] S. G. Warren, Optical constants of carbon dioxide ice 25 (1986) 2650–2674.
- [14] Hansen, The infrared absorption spectrum of carbon dioxide ice from 1.8 to 333  $\mu\text{m}$ , *Journal of Geophysical Research: Planets* 102 (1997) 21569–21587.
- [15] Hansen, Ultraviolet to near-infrared absorption spectrum of carbon dioxide ice from 0.174 to 1.8  $\mu\text{m}$ , *Journal of Geophysical Research: Planets* 110 (2005).
- [16] C. F. Bohren, B. R. Barkstrom, Theory of the optical properties of snow, *Journal of Geophysical Research* 79 (1974) 4527–4535.
- [17] W. J. Wiscombe, S. G. Warren, A Model for the Spectral Albedo of Snow. I: Pure Snow., *Journal of Atmospheric Sciences* 37 (1980) 2712–2733.
- [18] B. Hapke, *Theory of reflectance and emittance spectroscopy*, 1993.
- [19] D. Singh, M. G. Flanner, An improved carbon dioxide snow spectral albedo model: Application to martian conditions, *Journal of Geophysical Research: Planets* 121 (2016) 2037–2054. 2016JE005040.
- [20] A. R. Khuller, P. R. Christensen, S. G. Warren, Spectral Albedo of Dusty Martian  $\text{H}_2\text{O}$  Snow and Ice, *Journal of Geophysical Research (Planets)* 126 (2021) e06910.

- [21] Z. Yoldi, A. Pommerol, B. Jost, O. Poch, J. Gouman, N. Thomas, Vis-  
nir reflectance of water ice/regolith analogue mixtures and implications  
for the detectability of ice mixed within planetary regoliths, *Geophysical  
Research Letters* 42 (2015) 6205–6212. 2015GL064780.
- [22] P. C. Thomas, M. C. Malin, P. B. James, B. A. Cantor, R. M. E.  
Williams, P. Gierasch, South polar residual cap of Mars: Features,  
stratigraphy, and changes 174 (2005) 535–559.
- [23] T. N. Titus, H. H. Kieffer, P. R. Christensen, Exposed water ice discov-  
ered near the south pole of mars, *Science* 299 (2003) 1048–1051.
- [24] J. J. Plaut, G. Picardi, A. Safaeinili, A. B. Ivanov, S. M. Milkovich,  
A. Cicchetti, W. Kofman, J. Mouginot, W. M. Farrell, R. J. Phillips,  
S. M. Clifford, A. Frigeri, R. Orosei, C. Federico, I. P. Williams, D. A.  
Gurnett, E. Nielsen, T. Hagfors, E. Heggy, E. R. Stofan, D. Plettmeier,  
T. R. Watters, C. J. Leuschen, P. Edenhofer, Subsurface Radar Sound-  
ing of the South Polar Layered Deposits of Mars, *Science* 316 (2007)  
92.
- [25] C. J. Bierson, R. J. Phillips, I. B. Smith, S. E. Wood, N. E. Putzig,  
D. Nunes, S. Byrne, Stratigraphy and evolution of the buried CO<sub>2</sub>  
deposit in the Martian south polar cap, *Geophysical Research Letters*  
43 (2016) 4172–4179.
- [26] J.-P. Bibring, Y. Langevin, F. Poulet, A. Gendrin, B. Gondet,  
M. Berthé, A. Soufflot, P. Drossart, M. Combes, G. Bellucci, V. Moroz,  
N. Mangold, B. Schmitt, OMEGA Team, S. Erard, O. Forni, N. Man-

- aud, G. Poulleau, T. Encrenaz, T. Fouchet, R. Melchiorri, F. Altieri, V. Formisano, G. Bonello, S. Fonti, F. Capaccioni, P. Cerroni, A. Coradini, V. Kottsov, N. Ignatiev, D. Titov, L. Zasova, P. Pinet, C. Sotin, E. Hauber, H. Hoffman, R. Jaumann, U. Keller, R. Arvidson, J. Mustard, T. Duxbury, F. Forget, Perennial water ice identified in the south polar cap of Mars, *Nature* 428 (2004) 627–630.
- [27] W. M. Calvin, T. Z. Martin, Spatial variability in the seasonal south polar cap of mars, *Journal of Geophysical Research: Planets* 99 (1994) 21143–21152.
- [28] H. H. Kieffer, T. N. Titus, K. F. Mullins, P. R. Christensen, Mars south polar spring and summer behavior observed by tes: Seasonal cap evolution controlled by frost grain size, *Journal of Geophysical Research: Planets* 105 (2000) 9653–9699.
- [29] H. H. Kieffer, Cold jets in the Martian polar caps, *Journal of Geophysical Research (Planets)* 112 (2007) E08005.
- [30] Y. Langevin, J.-P. Bibring, F. Montmessin, F. Forget, M. Vincendon, S. Douté, F. Poulet, B. Gondet, Observations of the south seasonal cap of mars during recession in 2004–2006 by the omega visible/near-infrared imaging spectrometer on board mars express, *Journal of Geophysical Research: Planets* 112 (2007) n/a–n/a. E08S12.
- [31] S. Murchie, R. Arvidson, P. Bedini, K. Beisser, J. P. Bibring, J. Bishop, J. Boldt, P. Cavender, T. Choo, R. T. Clancy, E. H. Darlington, D. Des Marais, R. Espiritu, D. Fort, R. Green, E. Guinness, J. Hayes, C. Hash,

- K. Heffernan, J. Hemmler, G. Heyler, D. Humm, J. Hutcheson, N. Izenberg, R. Lee, J. Lees, D. Lohr, E. Malaret, T. Martin, J. A. McGovern, P. McGuire, R. Morris, J. Mustard, S. Pelkey, E. Rhodes, M. Robinson, T. Roush, E. Schaefer, G. Seagrave, F. Seelos, P. Silverglate, S. Slavney, M. Smith, W. J. Shyong, K. Strohhahn, H. Taylor, P. Thompson, B. Tossman, M. Wirzburger, M. Wolff, Compact Reconnaissance Imaging Spectrometer for Mars (CRISM) on Mars Reconnaissance Orbiter (MRO), *Journal of Geophysical Research (Planets)* 112 (2007) E05S03.
- [32] J. F. Bell, M. J. Wolff, M. C. Malin, W. M. Calvin, B. A. Cantor, M. A. Caplinger, R. T. Clancy, K. S. Edgett, L. J. Edwards, J. Fahle, F. Ghaemi, R. M. Haberle, A. Hale, P. B. James, S. W. Lee, T. McConnochie, E. Noe Dobrea, M. A. Ravine, D. Schaeffer, K. D. Supulver, P. C. Thomas, Mars Reconnaissance Orbiter Mars Color Imager (MARCI): Instrument description, calibration, and performance, *Journal of Geophysical Research (Planets)* 114 (2009) E08S92.
- [33] A. J. Brown, W. M. Calvin, P. C. McGuire, S. L. Murchie, Compact reconnaissance imaging spectrometer for mars (crism) south polar mapping: First mars year of observations, *Journal of Geophysical Research: Planets* 115 (2010).
- [34] A. S. McEwen, E. M. Eliason, J. W. Bergstrom, N. T. Bridges, C. J. Hansen, W. A. Delamere, J. A. Grant, V. C. Gulick, K. E. Herkenhoff, L. Keszthelyi, R. L. Kirk, M. T. Mellon, S. W. Squyres, N. Thomas, C. M. Weitz, Mars reconnaissance orbiter's high resolution imaging

- science experiment (hirise), *Journal of Geophysical Research: Planets* 112 (????).
- [35] A. Pommerol, G. Portyankina, N. Thomas, K.-M. Aye, C. J. Hansen, M. Vincendon, Y. Langevin, Evolution of south seasonal cap during martian spring: Insights from high-resolution observations by hirise and crism on mars reconnaissance orbiter, *Journal of Geophysical Research: Planets* 116 (2011) n/a–n/a. E08007.
- [36] A. J. Brown, S. Piqueux, T. N. Titus, Interannual observations and quantification of summertime h<sub>2</sub>O ice deposition on the martian CO<sub>2</sub> ice south polar cap, *Earth and Planetary Science Letters* 406 (2014) 102–109.
- [37] P. R. Christensen, B. M. Jakosky, H. H. Kieffer, M. C. Malin, J. McSween, Harry Y., K. Neelson, G. L. Mehall, S. H. Silverman, S. Ferry, M. Caplinger, M. Ravine, The Thermal Emission Imaging System (THEMIS) for the Mars 2001 Odyssey Mission, *Space Science Reviews* 110 (2004) 85–130.
- [38] P. R. Christensen, J. L. Bandfield, V. E. Hamilton, S. W. Ruff, H. H. Kieffer, T. N. Titus, M. C. Malin, R. V. Morris, M. D. Lane, R. L. Clark, B. M. Jakosky, M. T. Mellon, J. C. Pearl, B. J. Conrath, M. D. Smith, R. T. Clancy, R. O. Kuzmin, T. Roush, G. L. Mehall, N. Gorelick, K. Bender, K. Murray, S. Dason, E. Greene, S. Silverman, M. Greenfield, Mars Global Surveyor Thermal Emission Spectrometer experiment: Investigation description and surface science results, *Journal of Geophysical Research* 106 (2001) 23823–23872.

- [39] K. L. Wagstaff, T. N. Titus, A. B. Ivanov, R. Castaño, J. L. Bandfield, Observations of the north polar water ice annulus on Mars using THEMIS and TES, *Planetary and Space Science* 56 (2008) 256–265.
- [40] H. Houben, R. M. Haberle, R. E. Young, A. P. Zent, Modeling the Martian seasonal water cycle, *Journal of Geophysical Research* 102 (1997) 9069–9084.
- [41] Y. Langevin, F. Poulet, J.-P. Bibring, B. Schmitt, S. Douté, B. Gondet, Summer evolution of the north polar cap of mars as observed by omega/mars express, *Science* 307 (2005) 1581–1584.
- [42] T. Appéré, B. Schmitt, Y. Langevin, S. Douté, A. Pommerol, F. Forget, A. Spiga, B. Gondet, J.-P. Bibring, Winter and spring evolution of northern seasonal deposits on mars from omega on mars express, *Journal of Geophysical Research: Planets* 116 (2011) n/a–n/a. E05001.
- [43] C. Hansen, S. Byrne, G. Portyankina, M. Bourke, C. Dundas, A. McEwen, M. Mellon, A. Pommerol, N. Thomas, Observations of the northern seasonal polar cap on mars: I. spring sublimation activity and processes, *Icarus* 225 (2013) 881 – 897. Mars Polar Science V.
- [44] G. Portyankina, A. Pommerol, K.-M. Aye, C. J. Hansen, N. Thomas, Observations of the northern seasonal polar cap on mars ii: Hirise photometric analysis of evolution of northern polar dunes in spring, *Icarus* 225 (2013) 898 – 910. Mars Polar Science V.
- [45] A. Pommerol, T. Appéré, G. Portyankina, K.-M. Aye, N. Thomas, C. Hansen, Observations of the northern seasonal polar cap on mars

- iii: Crism/hirise observations of spring sublimation, *Icarus* 225 (2013) 911 – 922. Mars Polar Science V.
- [46] E. Quirico, B. Schmitt, Near-infrared spectroscopy of simple hydrocarbons and carbon oxides diluted in solid  $n_2$  and as pure ices: Implications for triton and pluto, *Icarus* 127 (1997) 354 – 378.
- [47] K. I. Öberg, H. J. Fraser, A. C. A. Boogert, S. E. Bisschop, G. W. Fuchs, E. F. van Dishoeck, H. Linnartz, Effects of  $CO_2$  on  $H_2O$  band profiles and band strengths in mixed  $H_2O:CO_2$  ices, *Astronomy and Astrophysics* 462 (2007) 1187–1198.
- [48] H. H. Kieffer, Near infrared spectral reflectance of simulated Martian frosts, Ph.D. thesis, California Institute of Technology, United States, 1968.
- [49] H. Kieffer, Spectral reflectance of  $CO_2$ - $H_2O$  frosts, *Journal of Geophysical Research* 75 (1970) 501–509.
- [50] M. P. Bernstein, D. P. Cruikshank, S. A. Sandford, Near-infrared laboratory spectra of solid  $H_2O/CO_2$  and  $CH_3OH/CO_2$  ice mixtures, *Icarus* 179 (2005) 527–534.
- [51] A. Oancea, O. Grasset, E. Le Menn, O. Bollengier, L. Bezacier, S. Le Mouélic, G. Tobie, Laboratory infrared reflection spectrum of carbon dioxide clathrate hydrates for astrophysical remote sensing applications, *Icarus* 221 (2012) 900–910.
- [52] F. Grisolle, T. Appéré, B. Schmitt, P. Beck, O. Brissaud, S. Douté,

- Influence of condensing water frost on the near-ir spectrum of  $\text{CO}_2$  snow (2011).
- [53] S. Philippe, B. Schmitt, P. Beck, O. Brissaud, Sublimation of  $\text{CO}_2$  ice with  $\text{H}_2\text{O}$  ice contamination: analogy with the sublimation of mars seasonal caps (2015).
- [54] B. Schmitt, S. Philippe, P. Beck, O. Brissaud, Sublimation at grain boundaries of polycrystalline  $\text{CO}_2$  slab ice: the clue to the strong spring albedo increase of the martian seasonal polar caps (2020).
- [55] G. Portyankina, J. Merrison, J. Iversen, Z. Yoldi, C. Hansen, K.-M. Aye, A. Pommerol, N. Thomas, Laboratory investigations of the physical state of  $\text{CO}_2$  ice in a simulated martian environment, *Icarus* 322 (2019) 210 – 220.
- [56] Z. Yoldi, A. Pommerol, O. Poch, N. Thomas, Reflectance study of ice and mars soil simulant associations – i.  $\text{H}_2\text{O}$  ice, *Icarus* (2020) 114169.
- [57] A. Pommerol, B. Jost, O. Poch, Z. Yoldi, Y. Brouet, A. Gracia-Berná, R. Cerubini, A. Galli, P. Wurz, B. Gundlach, J. Blum, N. Carrasco, C. Szopa, N. Thomas, Experimenting with mixtures of water ice and dust as analogues for icy planetary material, *Space Science Reviews* 215 (2019) 37.
- [58] F. Forget, G. B. Hansen, J. B. Pollack, Low brightness temperatures of martian polar caps:  $\text{CO}_2$  clouds or low surface emissivity?, *Journal of Geophysical Research: Planets* 100 (1995) 21219–21234.

- [59] H. H. Kieffer, P. R. Christensen, T. N. Titus,  $\text{CO}_2$  jets formed by sublimation beneath translucent slab ice in Mars' seasonal south polar ice cap, *Nature* 442 (2006).
- [60] Y. Brouet, Contribution à la détermination de la permittivité des noyaux cométaires et des astéroïdes, 2013.
- [61] C. C. Allen, R. V. Morris, D. J. Lindstrom, M. M. Lindstrom, J. P. Lockwood, JSC Mars-1: Martian regolith simulant, *Lunar and Planetary Science XXVIII* (1997).
- [62] M. J. Wolff, M. D. Smith, R. T. Clancy, R. Arvidson, M. Kahre, F. See-los IV, S. Murchie, H. Savijärvi, Wavelength dependence of dust aerosol single scattering albedo as observed by the compact reconnaissance imaging spectrometer, *Journal of Geophysical Research: Planets* 114 (2009).
- [63] W. Goetz, W. T. Pike, S. F. Hviid, M. B. Madsen, R. V. Morris, M. H. Hecht, U. Staufer, K. Leer, H. Sykulka, E. Hemmig, J. Marshall, J. M. Morookian, D. Parrat, S. Vijendran, B. J. Bos, M. R. El Maarry, H. U. Keller, R. Kramm, W. J. Markiewicz, L. Drube, D. Blaney, R. E. Arvidson, J. F. Bell III, R. Reynolds, P. H. Smith, P. Woida, R. Woida, R. Tanner, Microscopy analysis of soils at the Phoenix landing site, Mars: Classification of soil particles and description of their optical and magnetic properties, *Journal of Geophysical Research: Planets* 115 (2010).
- [64] A. Pommerol, B. Jost, O. Poch, M. El-Maarry, B. Vuitel, N. Thomas, The Sciteas experiment: Optical characterizations of sublimating icy

- planetary analogues, *Planetary and Space Science* 109–110 (2015) 106–122.
- [65] R. Cerubini, A. Pommerol, Z. Yoldi, N. Thomas, Near-infrared reflectance spectroscopy of sublimating salty ice analogues. implications for icy moons, *Planetary and Space Science* 211 (2022) 105391.
- [66] D. G. Blackburn, K. L. Bryson, V. F. Chevrier, L. A. Roe, K. F. White, Sublimation kinetics of co<sub>2</sub> ice on mars, *Planetary and Space Science* 58 (2010) 780–791.
- [67] R. N. Clark, P. G. Lucey, Spectral Properties of Ice Mineral Mixtures: Implications on the Composition on the Galilean Satellites and Other Icy Bodies., in: *Bulletin of the American Astronomical Society*, volume 13, p. 700.
- [68] S.-M. Li, K.-S. Yang, C.-C. Wang, A semi-empirical model for predicting frost properties, *Processes* 9 (2021).
- [69] Fornasier, S., Hasselmann, P. H., Barucci, M. A., Feller, C., Besse, S., Leyrat, C., Lara, L., Gutierrez, P. J., Oklay, N., Tubiana, C., Scholten, F., Sierks, H., Barbieri, C., Lamy, P. L., Rodrigo, R., Koschny, D., Rickman, H., Keller, H. U., Agarwal, J., A´Hearn, M. F., Bertaux, J.-L., Bertini, I., Cremonese, G., Da Deppo, V., Davidsson, B., Debei, S., De Cecco, M., Fulle, M., Groussin, O., Güttler, C., Hviid, S. F., Ip, W., Jorda, L., Knollenberg, J., Kovacs, G., Kramm, R., Kührt, E., Küppers, M., La Forgia, F., Lazzarin, M., Lopez Moreno, J. J., Marzari, F., Matz, K.-D., Michalik, H., Moreno, F., Mottola, S., Naletto, G., Pa-

jola, M., Pommerol, A., Preusker, F., Shi, X., Snodgrass, C., Thomas, N., Vincent, J.-B., Spectrophotometric properties of the nucleus of comet 67p/churyumov-gerasimenko from the osiris instrument onboard the rosetta spacecraft, *A&A* 583 (2015) A30.

- [70] N. Thomas, G. Cremonese, R. Ziethe, M. Gerber, M. Brändli, G. Bruno, M. Erismann, L. Gambicorti, T. Gerber, K. Ghose, M. Gruber, P. Gubler, H. Mischler, J. Jost, D. Piazza, A. Pommerol, M. Rieder, V. Roloff, A. Servonet, W. Trottmann, T. Uthaicharoenpong, C. Zimmermann, D. Vernani, M. Johnson, E. Pelò, T. Weigel, J. Viertl, N. De Roux, P. Lochmatter, G. Sutter, A. Casciello, T. Hausner, I. Fikai Veltroni, V. Da Deppo, P. Orleanski, W. Nowosielski, T. Zawistowski, S. Szalai, B. Sodor, S. Tulyakov, G. Troznai, M. Banaskiewicz, J. C. Bridges, S. Byrne, S. Debei, M. R. El-Maarry, E. Hauber, C. J. Hansen, A. Ivanov, L. Keszthelyi, R. Kirk, R. Kuzmin, N. Mangold, L. Marinangeli, W. J. Markiewicz, M. Massironi, A. S. McEwen, C. Okubo, L. L. Tornabene, P. Wajer, J. J. Wray, The colour and stereo surface imaging system (cassis) for the exomars trace gas orbiter, *Space Science Reviews* 212 (2017) 1897–1944.
- [71] S. G. Warren, W. J. Wiscombe, J. F. Firestone, Spectral albedo and emissivity of CO<sub>2</sub> in Martian polar caps: model results., *Journal of Geophysical Research* 95 (1990) 14717–14741.
- [72] O. Poch, A. Pommerol, B. Jost, N. Carrasco, C. Szopa, N. Thomas, Sublimation of water ice mixed with silicates and tholins: Evolution of

surface texture and reflectance spectra, with implications for comets, *Icarus* 267 (2016) 154 – 173.

- [73] J. Eluszkiewicz, J.-L. Moncet, T. N. Titus, G. B. Hansen, A microphysically-based approach to modeling emissivity and albedo of the martian seasonal caps, *Icarus* 174 (2005) 524 – 534. *Mars Polar Science III*.